



## BIROn - Birkbeck Institutional Research Online

Atherton, Joe and Hummel, J.J.A. and Olieric, N. and Locke, J. and Peña, A. and Rosenfeld, S. and Steinmetz, M. and Hoogenraad, C.C. and Moores, Carolyn A. (2020) The mechanism of kinesin inhibition by kinesin binding protein. *eLife* , ISSN 2050-084X.

Downloaded from: <https://eprints.bbk.ac.uk/id/eprint/41854/>

*Usage Guidelines:*

Please refer to usage guidelines at <https://eprints.bbk.ac.uk/policies.html>

or alternatively

contact [lib-eprints@bbk.ac.uk](mailto:lib-eprints@bbk.ac.uk).

# The mechanism of kinesin inhibition by kinesin-binding protein

Joseph Atherton<sup>1,2\*</sup>, Jessica JA Hummel<sup>3</sup>, Natacha Olieric<sup>4</sup>, Julia Locke<sup>2†</sup>, Alejandro Peña<sup>2‡</sup>, Steven S Rosenfeld<sup>5</sup>, Michel O Steinmetz<sup>4,6</sup>, Casper C Hoogenraad<sup>3</sup>, Carolyn A Moores<sup>2</sup>

<sup>1</sup>Randall Centre for Cell and Molecular Biophysics, King's College, London, United Kingdom; <sup>2</sup>Institute of Structural and Molecular Biology, Birkbeck, University of London, London, United Kingdom; <sup>3</sup>Cell Biology, Neurobiology and Biophysics, Department of Biology, Faculty of Science, Utrecht University, Utrecht, Netherlands; <sup>4</sup>Laboratory of Biomolecular Research, Division of Biology and Chemistry, Paul Scherrer Institut, Villigen PSI, Switzerland; <sup>5</sup>Department of Cancer Biology, Mayo Clinic, Jacksonville, United States; <sup>6</sup>University of Basel, Biozentrum, Basel, Switzerland

**\*For correspondence:**

joseph.atherton@kcl.ac.uk

**Present address:**

<sup>†</sup>Macromolecular Machines Laboratory, The Francis Crick Institute, London, United Kingdom; <sup>‡</sup>Department of In Silico Drug Discovery, Pharmidex Pharmaceuticals, Hatfield, United Kingdom

**Competing interests:** The

authors declare that no competing interests exist.

**Funding:** See page 25

**Received:** 27 July 2020

**Accepted:** 28 November 2020

**Published:** 30 November 2020

**Reviewing editor:** Andrew P

Carter, MRC Laboratory of Molecular Biology, United Kingdom

© Copyright Atherton et al. This article is distributed under the terms of the [Creative Commons Attribution License](https://creativecommons.org/licenses/by/4.0/), which permits unrestricted use and redistribution provided that the original author and source are credited.

**Abstract** Subcellular compartmentalisation is necessary for eukaryotic cell function. Spatial and temporal regulation of kinesin activity is essential for building these local environments via control of intracellular cargo distribution. Kinesin-binding protein (KBP) interacts with a subset of kinesins via their motor domains, inhibits their microtubule (MT) attachment, and blocks their cellular function. However, its mechanisms of inhibition and selectivity have been unclear. Here we use cryo-electron microscopy to reveal the structure of KBP and of a KBP–kinesin motor domain complex. KBP is a tetratricopeptide repeat-containing, right-handed  $\alpha$ -solenoid that sequesters the kinesin motor domain's tubulin-binding surface, structurally distorting the motor domain and sterically blocking its MT attachment. KBP uses its  $\alpha$ -solenoid concave face and edge loops to bind the kinesin motor domain, and selected structure-guided mutations disrupt KBP inhibition of kinesin transport in cells. The KBP-interacting motor domain surface contains motifs exclusively conserved in KBP-interacting kinesins, suggesting a basis for kinesin selectivity.

## Introduction

Kinesins are a superfamily of microtubule (MT)-based molecular motors that play important roles in cellular functions such as mitosis, cell motility, and intracellular transport (Vale, 2003; Hirokawa et al., 2009; Klinman and Holzbaaur, 2018). Kinesins are categorised into 14 sub-classes (kinesin-1 to kinesin-14 [Lawrence et al., 2004]) by motor domain conservation and within these sub-classes individual family members (a total of 45 'KIF' or 'Kif' genes in humans and mice respectively) have a wide range of functional characteristics and biological roles (Vale, 2003; Miki et al., 2001). Dysfunction of kinesin family members has been implicated in a number of pathological conditions (Hirokawa et al., 2010; Mandelkow and Mandelkow, 2002). The kinesin motor domain is the MT-binding engine that drives these activities, converting the chemical energy of ATP binding and hydrolysis into mechanical force. While these mechanical forces are classically used to generate motility in transport kinesins, some kinesin family members drive MT organisation or depolymerisation of MTs.

Kinesins are highly regulated in order to prevent both waste of ATP and to spatially and temporally control kinesin function. This is particularly important in highly polarised and compartmentalised cells such as neurons. Kinesin regulation via inhibition of their motor domains can occur through a number of mechanisms that limit ATPase activity and/or block track binding – these include

intramolecular inhibition by kinesin tail domains, post-translational modification of the motor, or through interactions with regulatory binding partners. Recently, it has been demonstrated that a subset of kinesin superfamily members, including kinesin-2s, -3 s, -8 s, and -12 s, are sequestered by kinesin-binding protein (KBP; KIF1BP; KIAA1279), which inhibits MT track attachment by their motor domains and, thus, blocks their MT-related functions (Wozniak *et al.*, 2005; Kevenaar *et al.*, 2016; Alves *et al.*, 2010).

KBP is expressed in multiple human tissues including brain and heart (Wozniak *et al.*, 2005). Mutations in the KBP have been identified as causing autosomal recessive Goldberg-Shprintzen syndrome (GOSHS) (Brooks *et al.*, 2005; Dafsari *et al.*, 2015; Valence *et al.*, 2013; Salehpour *et al.*, 2017), which presents as congenital facial dysmorphism, nervous system pathology, and dysfunction and heart defects (Tanaka *et al.*, 1993). In addition, KBP gene copy number has been recently reported as predictive in paediatric neuroblastoma prognosis, prompting its suggestion as a drug target (Suo *et al.*, 2018). KBP was originally identified as a kinesin-3-binding partner that modulated its mitochondrial transport function (Wozniak *et al.*, 2005); however, KBP has since been shown to interact with a subset of other kinesin family members to regulate diverse cellular processes including mitosis (Brouwers *et al.*, 2017; Malaby *et al.*, 2019), spermatogenesis (Lehti *et al.*, 2015), and neuronal differentiation, growth, and cargo distribution (Alves *et al.*, 2010; Lyons *et al.*, 2008; Drévilion *et al.*, 2013; Drerup *et al.*, 2016; Chang *et al.*, 2019; Hirst *et al.*, 2017).

We do not currently know what the structure of KBP is, nor understand the mechanism of KBP–kinesin inhibition. It is also completely unknown how KBP differentiates between particular kinesin family members. KBP is a 72 kDa protein, is predicted to contain several tetratricopeptide repeats (TPRs), and to be mainly  $\alpha$ -helical in secondary structure content (Wozniak *et al.*, 2005; Kevenaar *et al.*, 2016). Here we present cryo-electron microscopy (cryo-EM) structures of KBP alone and of KBP bound to the motor domain of the human mitotic kinesin KIF15 (a 110 kDa complex). We show that KBP is a TPR-containing, right-handed  $\alpha$ -solenoid protein composed of nine antiparallel  $\alpha$ -helix pairs interrupted by a linker region. We also show that KBP's concave face binds KIF15 via its MT-binding elements and induces a large displacement of the kinesin  $\alpha$ 4 helix, sterically inhibiting MT association. Finally, we show that KBP's kinesin selectivity is associated with specific kinesin sequences spread across the interaction surface.

## Results

### KBP is a TPR-containing, right-handed $\alpha$ -solenoid

The 3D structure of the ~72 kDa KBP at 4.6 Å resolution (Figure 1 and Figure 1—figure supplement 1a and b) was determined using cryo-EM data collected using a Volta phase plate (VPP), and an atomic model was calculated (see Materials and methods Table 1). Our structure revealed that KBP is a right-handed  $\alpha$ -solenoid protein (Figure 1a and b and Figure 1—figure supplement 1c–e). Nine pairs of anti-parallel  $\alpha$ -helices ( $\alpha$ HP1 [ $\alpha$ -helical pair 1] to  $\alpha$ HP9) are broken by a single 'linker  $\alpha$ -helix' (L $\alpha$ H) and 'linker loop' (LL) in the centre of the fold separating KBP into N-terminal and C-terminal subdomains (Figure 1, Figure 1—figure supplement 1c–e, and Figure 1—figure supplement 2). The four predicted TPR motifs contribute exclusively to  $\alpha$ -helical pairs in the N-terminal subdomain (Figure 1a,d, and e).

The supercoiling  $\alpha$ -helical pairs form concave and convex faces linked by short and long loops that constitute the two edges of the  $\alpha$ -solenoid (Figure 1—figure supplement 1c–e and Figure 1—figure supplement 2). In contrast to the shorter loops, the longer loops (more than seven residues) tend to be partially disordered, show low sequence homology between KBP orthologues in different species, and are mainly found in the N-terminal subdomain (e.g. L2, L6, and L10; Figure 1—figure supplement 1d and e and Figure 1—figure supplement 2). The LL is the longest (62 residues) and is thus unique in the KBP structure because it is reasonably conserved and mainly ordered, with visible corresponding density clearly bridging the N- and C-terminal subdomains (Figure 1a and b, Figure 1—figure supplement 1d and e, Figure 1—figure supplement 2, and Figure 1—figure supplement 3). Despite this clear ordered density, this loop was not modelled due to low homology to available structures and a lack of consensus in secondary structure prediction (see Materials and methods). In spite of this lack of consensus, density in this region suggests that part of this loop may form further  $\alpha$ -helical structures. Other TPR-containing  $\alpha$ -solenoid proteins form

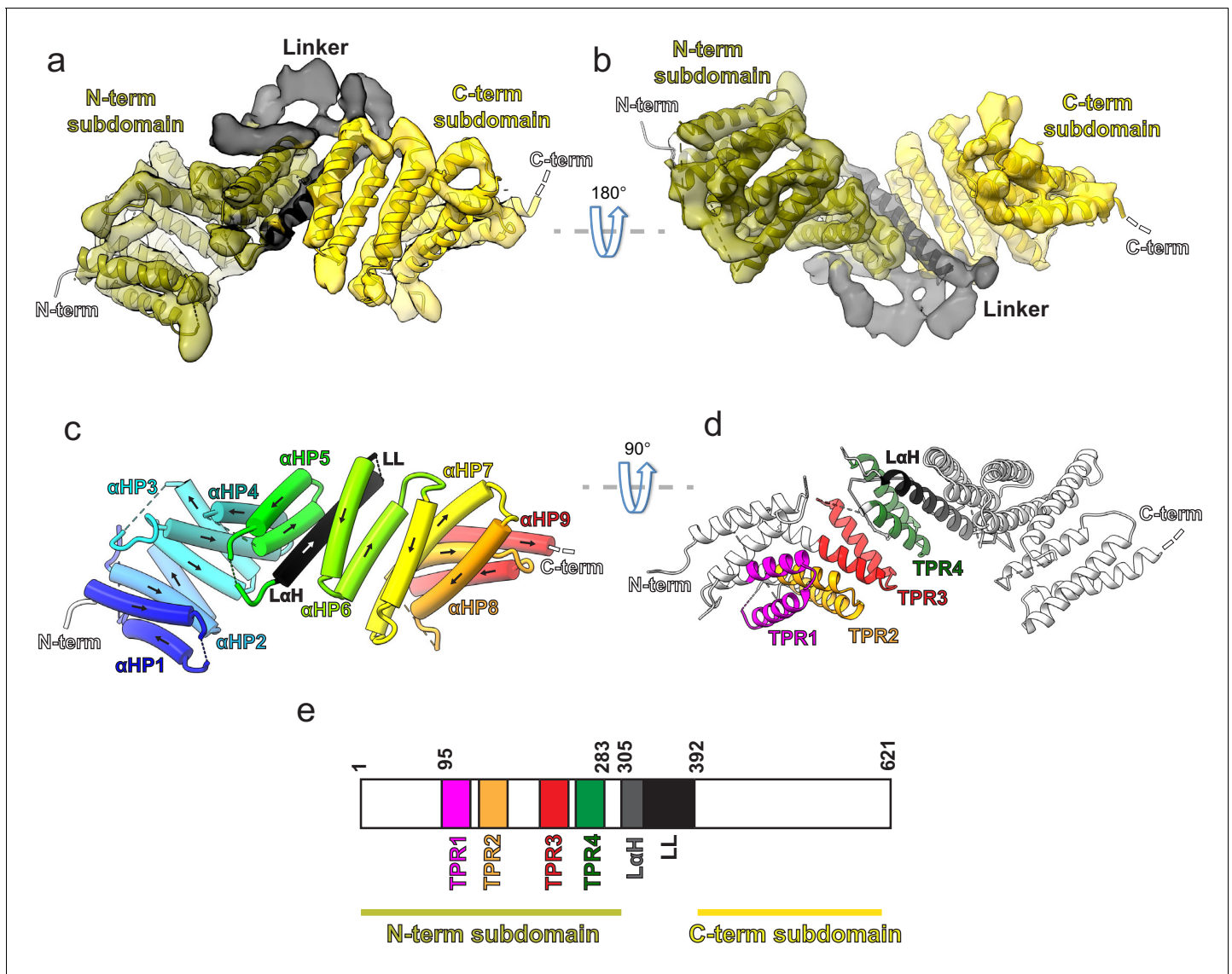


**Figure 1.** Kinesin-binding protein (KBP) is a tetratricopeptide repeat (TPR)-containing right-handed  $\alpha$ -solenoid. (a) Model of KBP (ribbon representation) displayed in experimental cryo-electron microscopy density. The N-terminal (olive) and C-terminal (gold) subdomains are separated by a linker region (black). Semi-transparent density is coloured regionally as per the fitted model. The N- and C-termini are shown, with a dotted line representing the disordered C-terminus (not modelled). The linker loop (LL) region was not modelled but its density is shown in semi-transparent black. (b) The same as panel a, but rotated 180° around the axis indicated. (c) The same view as in panel a, but with the density removed and  $\alpha$ -helices displayed as pipes with their directionality indicated by arrows. The nine antiparallel  $\alpha$ -helical pairs ( $\alpha$ HP1– $\alpha$ HP9) are each coloured separately and labelled, as is the linker  $\alpha$ -helix (L $\alpha$ H) and LL (dotted line). (d) Ribbon representation of KBP showing the four TPR motifs and the L $\alpha$ H coloured according to the labels. View related to panel c, by a 90° rotation around the indicated axis. (e) Schematic of the KBP showing the position of the TPR motifs between residue 95 and 283 of the N-terminal subdomain and position of the linker region (L $\alpha$ H and LL) between residues 305 and 392. The online version of this article includes the following figure supplement(s) for figure 1:

**Figure supplement 1.** Kinesin-binding protein (KBP) reconstruction, structure, and loop lengths.

**Figure supplement 2.** Kinesin-binding protein (KBP) loops, sequence, inter-species conservation, and experimental mutations.

**Figure supplement 3.** Approximate path of the kinesin-binding protein (KBP) linker loop (LL).

**Table 1.** Cryo-electron microscopy reconstruction information and model refinement statistics and model geometry. Data collection, processing, and model refinement information for the kinesin-binding protein (KBP), KBP–KIF15\_MD6S, and KIF15\_MD6S–MT datasets.

	KBP (EMDB: EMD-11338, PDB: 6ZPG)	KBP–KIF15_MD6S (EMDB: EMD-11339, PDB: 6ZPH)	KIF15_MD6S–MT (EMDB: EMD-11340, PDB: 6ZPI)
Data collection and processing			
Pixel size (Å)*	1.055, 1.043, or 1.047	1.047	1.39
Number of micrographs (collected, final)*	9360, 7547	6497, 5138	214,202
Final particle number	258,049 (81,628 of which on graphene oxide)	7513	12,674
Map resolution (Å) FSC threshold†	4.6 Independent half-map FSC 0.143	6.9 Independent half-map FSC 0.143	4.5 Independent half-map FSC 0.143
Refinement			
Refinement resolution (Å) CC_mask‡	4.6 0.64	6.9 0.74	6 0.60
Map sharpening <i>B</i> -factor (Å <sup>2</sup> )	–200	–495	–134
Model composition	3808	6232	9420
Nonhydrogen atoms	610	948	1185
Protein residues	0	1	4
Ligands			
R.m.s. deviations§	0.01	0.01	0.08
Bond lengths (Å)	0.96	1.07	0.17
Bond angles (°)			
Validation#	1.66	1.84	1.95
MolProbity score	5.25	7.31	13.25
Clashscore	0.5%	0.9%	0.1%
Poor rotamers (%)			
Ramachandran plot#	94.38	93.13	95.38
Favoured (%)	5.62	6.87	4.62
Allowed (%)	0	0	0
Outliers (%)			

\*Inclusive of all data collection sessions.

†The resolution value at the gold-standard Fourier Shell Correlation (FSC) 0.143 criterion between independently refined half-maps.

‡Cross-correlation provided by Phenix real-space refine (Afonine et al., 2018).

§Root-mean-square deviations of bond lengths or angles in the model.

#As defined by the MolProbity validation server (Chen et al., 2010).

important regulatory interactions in numerous contexts, and the structure we describe is indicative of similar properties for KBP.

### KBP conformationally adapts to bind KIF15's motor domain using both subdomains

To elucidate the mechanism of kinesin inhibition by KBP, we determined the structure of KBP in complex with the human KIF15 (kinesin-12) motor domain (KIF15\_MD, 1–375). This construct, which has six of its eight cysteine residues mutated to serine (C5S, C50S, C162S, C294S, C314S, and C346S) and two additional cysteines were inserted (S250C and G375C), has comparable steady-state ATPase activity to previously published reports (Klejnot et al., 2014; Figure 2—figure supplement 1a) and we refer to it as KIF15\_MD6S. The overall resolution of this KBP–KIF15\_MD6S complex was 6.9 Å, with KBP and KIF15\_MD6S determined to similar local resolutions (Figure 2—figure supplement 1b and c). We built a model of the complex via flexible fitting using our KBP model and the KIF15\_MD crystal structure (Figure 2a and b, Table 1 and see Materials and methods). The complex is arranged such that KIF15\_MD6S sits in the concave face of the KBP  $\alpha$ -solenoid, analogous to

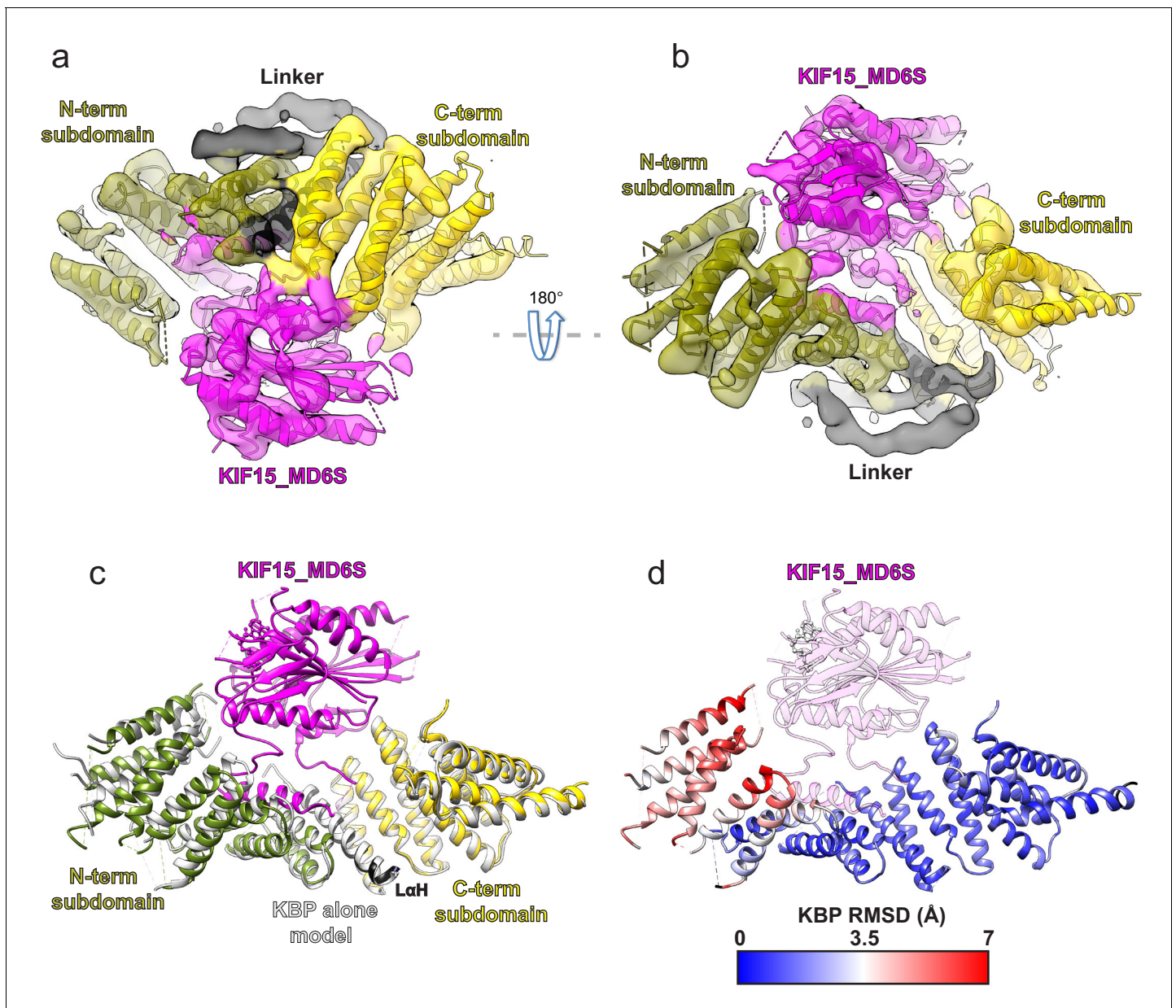


**Figure 2.** Kinesin-binding protein (KBP) conformationally adapts to bind KIF15's motor domain via both subdomains. (a) Model of the KBP–KIF15\_MD6S complex (ribbon representation) displayed in experimental cryo-electron microscopy density. The N-terminal (olive) and C-terminal (gold) subdomains and the linker helix (black) are shown in KBP, while kinesin is coloured in magenta. Semi-transparent density is coloured regionally as per the fitted model and additional density for the linker loop is shown in semi-transparent black. (b) The same as panel a, but rotated 180° around the axis indicated. (c) The KBP-alone model (light grey ribbons) was superimposed on the KBP–KIF15\_MD6S model (opaque ribbons) using Chimera's matchmaker (Pettersen *et al.*, 2004). Colouring and view as in panel b. (d) RMSD in Å for KBP comparing KBP–KIF15\_MD6S and superimposed KBP-alone models as in panel c, shown on KBP from the KBP–KIF15\_MD6S model. Parts of the KBP model coloured black are disordered/missing in the KBP alone model. The KIF15\_MD6S is shown in transparent magenta.

The online version of this article includes the following figure supplement(s) for figure 2:

**Figure supplement 1.** Kinesin-binding protein (KBP)–KIF15\_MD6S reconstruction resolution estimation and 2D class analysis of KBP–KIF1A\_MD and KBP–KIF15\_MD complexes.

a baseball enclosed in a baseball glove. The kinesin MD is positioned centrally between the N- and C-terminal subdomains and contacts the KBP concave face and loops at the  $\alpha$ -solenoid edges.

When the structure of KBP-alone is superimposed onto KBP in the KBP–KIF15\_MD6S complex, it is clear that KBP undergoes a conformational change in the presence of its kinesin motor domain-

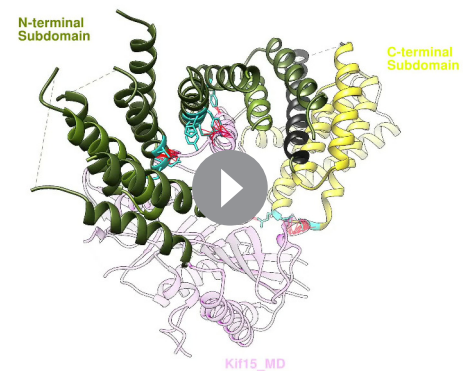
binding partner, with the largest differences resulting from an unfurling motion of its N-terminal subdomain (**Figure 2c and d** and **Video 1**). The KBP-alone model is incompatible with KIF15\_MD6S binding, due to clashes with L14 in the C-terminal subdomain and  $\alpha$ HP3a,  $\alpha$ HP4a, and L8 in the N-terminal subdomain. The conformational changes in KBP upon KIF15\_MD6S binding relieve these clashes in the complex (**Video 1**).

To establish whether the KBP–KIF15\_MD6S mode of interaction applied to other kinesins, we also collected data of the complex formed by KBP with the motor domain of the human kinesin-3 KIF1A (KIF1A\_MD). Two-dimensional classification of these images revealed a number of classes with an extra-density corresponding to the size of a kinesin motor domain bound to the concave face of KBP, consistent with what was observed in the KBP–KIF15\_MD6S dataset (**Figure 2—figure supplement 1c**). However, in contrast to the KBP–KIF15\_MD6S sample, these KBP–KIF1A\_MD 2D classes provided only limited views of the complex (**Figure 2—figure supplement 1c and d**), such that a reliable 3D structure could not be calculated. Intriguingly, in addition, the extra kinesin density in the 2D classes appeared to have a somewhat flexible position relative to KBP. However, these data did allow us to confirm that indeed KIF1A\_MD also interacts with KBP on its concave face in the same way as KIF15\_MD6S and suggests a common mechanism of kinesin inhibition by KBP.

### KIF15\_MD6S binds KBP via rearrangement of its tubulin-binding subdomain

We examined the effect of KBP binding on the conformation of KIF15\_MD6S. Kinesin motor domains can be structurally divided into three distinct subdomains (*Shang et al., 2014; Gigant et al., 2013*) which undergo coordinated conformational changes during the MT-based kinesin ATPase cycle. MT binding stabilises the tubulin-binding subdomain of the MD while the P-loop and Switch 1/2 subdomains – which contain the conserved nucleotide-coordinating P-loop and Switch 1 and 2 motifs – move relative to each other in response to the nucleotide state of the MD (*Shang et al., 2014; Gigant et al., 2013; Atherton et al., 2014*). We determined the structure of the MT-bound, AMPPNP state of KIF15\_MD6S, which shows that this MD adopts a canonical conformation (**Figure 3—figure supplement 1**). Comparison of this conformation with an ADP-bound Kif15\_MD crystal structure (PDB: 4BN2 *Klejnot et al., 2014*) illustrates the scale of these MT- and nucleotide-dependent subdomain rearrangements in KIF15, which are similar to those seen in other kinesins MDs (*Shang et al., 2014; Atherton et al., 2014; Atherton et al., 2017; Figure 3—figure supplement 1d and e and Figure 3c and d*).

The structure of the KBP–KIF15\_MD6S complex revealed that KBP binds the kinesin motor domain via the tubulin-binding subdomain (**Figure 3**). While the P-loop and Switch 1/2 subdomains of the KIF15\_MD crystal structure and associated  $Mg^{2+}$ -ADP generally fitted well into density of the KBP–KIF15\_MD6S complex, a large portion of the tubulin-binding subdomain did not (**Figure 3a** and **Figure 3—figure supplement 2a and b**). In particular, there is a striking lack of density in the expected position for helix



**Video 1.** Kinesin-binding protein (KBP) undergoes conformational change to relieve clashes when forming a complex with KIF15\_MD6S. The KBP-alone model was superimposed on the KBP–KIF15\_MD6S model using UCSF Chimera’s matchmaker (*Pettersen et al., 2004*). A conformational morph movie was then generated in Chimera between the KBP-alone and KIF15 motor domain bound states, with KIF15\_MD6S shown throughout to illustrate the relief of clashes. The N-terminal and C-terminal subdomains are coloured in olive and gold respectively, as in **Figure 2a and b**, while KIF15\_MD6S is shown in pale magenta. Distances between identified clashing atoms when KBP-alone is superimposed onto the KBP–KIF15\_MD6S model are indicated by red linking lines and KBP clashing residues and side chains shown in cyan. Atoms that were clashing remain coloured while the red lines gradually disappear as the clashes are relieved by the conformational change. Clashes were calculated in Chimera using default criteria.

<https://elifesciences.org/articles/61481#video1>

$\alpha 4$  (Figure 3a and Figure 3—figure supplement 2b). Instead, there was a strong density of length and width consistent with helix  $\alpha 4$  displaced by  $\sim 15$  Å into the concave face of KBP, which we modelled as such (Figure 3b and e, Figure 2, and Figure 3—figure supplement 2b–e). This displacement of helix  $\alpha 4$ , which lies close to the TPR-repeat region of the N-terminal subdomain of KBP, is accompanied by additional rearrangements of the flanking L11 and L12 in KIF15\_MD6S (labelled KL11 and KL12; Figure 3c–e and Figure 3—figure supplement 2b–e). A number of other TPR-containing  $\alpha$ -solenoids are known to bind peptide motifs with  $\alpha$ -helical content within their concave faces (Culurgioni et al., 2011; Wang et al., 2009; Quinaud et al., 2007; Figure 3—figure supplement 3), and our structure shows that KBP binds helix  $\alpha 4$  of KIF15\_MD6S in a similar way.

The KBP-bound conformation of the KIF15\_MD6S tubulin-binding subdomain is also radically different from its MT-bound conformation (Figure 3d and e). The tubulin-binding subdomain forms the majority of the MT-binding surface in the KIF15\_MD6S-MT complex (Figure 3d and Figure 3—figure supplement 1) such that KBP and MTs cannot simultaneously bind KIF15\_MD6S due to extensive steric overlap (Figure 3d and e). In summary, KBP sequesters and blocks the MT-interacting surface of kinesin motor domains via a mechanism that involves significant conformational change within the motor domain.

### **KBP binds kinesin motor domains via conserved motifs in the $\alpha$ -solenoid edge loops and $\alpha$ -helices at the concave face**

KBP contacts the KIF15\_MD6S both via (1) loops connecting the  $\alpha$ -solenoid edges and (2) TPR-containing  $\alpha$ -helices at the concave face (Figure 4, Figure 4—figure supplement 1, and Video 2). At the  $\alpha$ -solenoid edges, L1, L3, L5, and L10 in the N-terminal subdomain and L12, L14, L16, and L18 in the C-terminal subdomain are close enough to KIF15\_MD6S to be involved in binding. The closest interaction of these was KBP L12 and L14, which contact both K $\beta$ 5–KL8 and KL12–K $\alpha$ 5–KL13 regions of the KIF15 tubulin-binding subdomain (Figure 4). KBP's disordered L1 lies close to KIF15\_MD6S's KL9, while the shorter, ordered L3 and L5 are situated near but not contacting KL11 and K $\alpha$ 6 (Figure 4—figure supplement 1a and b). KBP's C-terminal L16 and L18 are close enough to KIF15\_MD6S that they may interact with the flexible KL12, N-terminus, or neck-linker. At the TPR-containing region of the concave face of KBP,  $\alpha$ HP4a,  $\alpha$ HP4b, and  $\alpha$ HP5a contact the K11–K $\alpha$ 4–KL12 region of KIF15\_MD6S (Figure 4c and d).

To test the functional significance of this interface, we investigated KBP–kinesin interactions in cells and examined the activities of mutant KBP constructs in which the predicted interacting amino acids within potentially kinesin-contacting loops were substituted for Ala, Gly, or Pro residues (Figure 1—figure supplement 2 and Table 2). Ala-substitutions in the TPR-containing  $\alpha$ -helices at the KBP concave face were also introduced at particularly inter-species conserved polar residues predicted to interact with the KIF15\_MD K11–K $\alpha$ 4–KL12 region (Tyr-213 and Gln-216 in  $\alpha$ HP4a, Gln-238 in  $\alpha$ HP4b, Thr-255 and Gln-258 in  $\alpha$ HP5a; Figure 4c and d and Figure 1—figure supplement 2). All mutant constructs exhibited roughly equivalent expression patterns that were also comparable to WT KBP (Figure 5—figure supplement 1).

We first used pull-down assays. Mouse Kif15 or Kif1A constructs consisting of only the motor domain and the first coiled-coil region (Kif15\_MDC or Kif1A\_MDC) were fused to bioGFP and co-expressed with various HA-tagged human KBP constructs in HEK293T cells, followed by pull-down of HA–KBP by the bioGFP–KIF\_MDC (Kevenaar et al., 2016; Figure 5—figure supplement 2). Although there are moderate qualitative differences in binding by the two motors, the effects of KBP mutations on motor binding – described in the following – are essentially the same. Ala-substitutions in the TPR-containing  $\alpha$ -helices at the KBP concave face ( $\alpha$ HP4a and  $\alpha$ HP4b), which lie at the heart of the KBP–KIF15\_MD6S structural interface, strongly reduced KBP's interaction with both KIF15\_MDC and KIF1A\_MDC.  $\alpha$ HP5a mutants had a similar but less pronounced effect (Figure 5—figure supplement 2b and c). In contrast, mutation of L1, L3, or L5 in the KBP N-terminal subdomain or L10 or L16 in the C-terminal subdomain – none of which form directly visualised interactions with KIF15\_MD6S in the cryo-EM reconstruction – has no effect on KBP's interaction with either KIF15\_MDC or KIF1A\_MDC (Figure 5—figure supplement 2b and c). Mutation of L12 (to some extent) and of L14 (to a greater extent) – which contact both K $\beta$ 5–KL8 and KL12–K $\alpha$ 5–KL13 – reduced KBP interaction with KIF15\_MDC and KIF1A\_MDC (Figure 5—figure supplement 2b and c). Mutation of L12 + L14 additively disrupted the KBP–motor interaction, consistent with the structural proximity of these two loops in the kinesin–KBP complex. L10 + L12 and L10 + L14

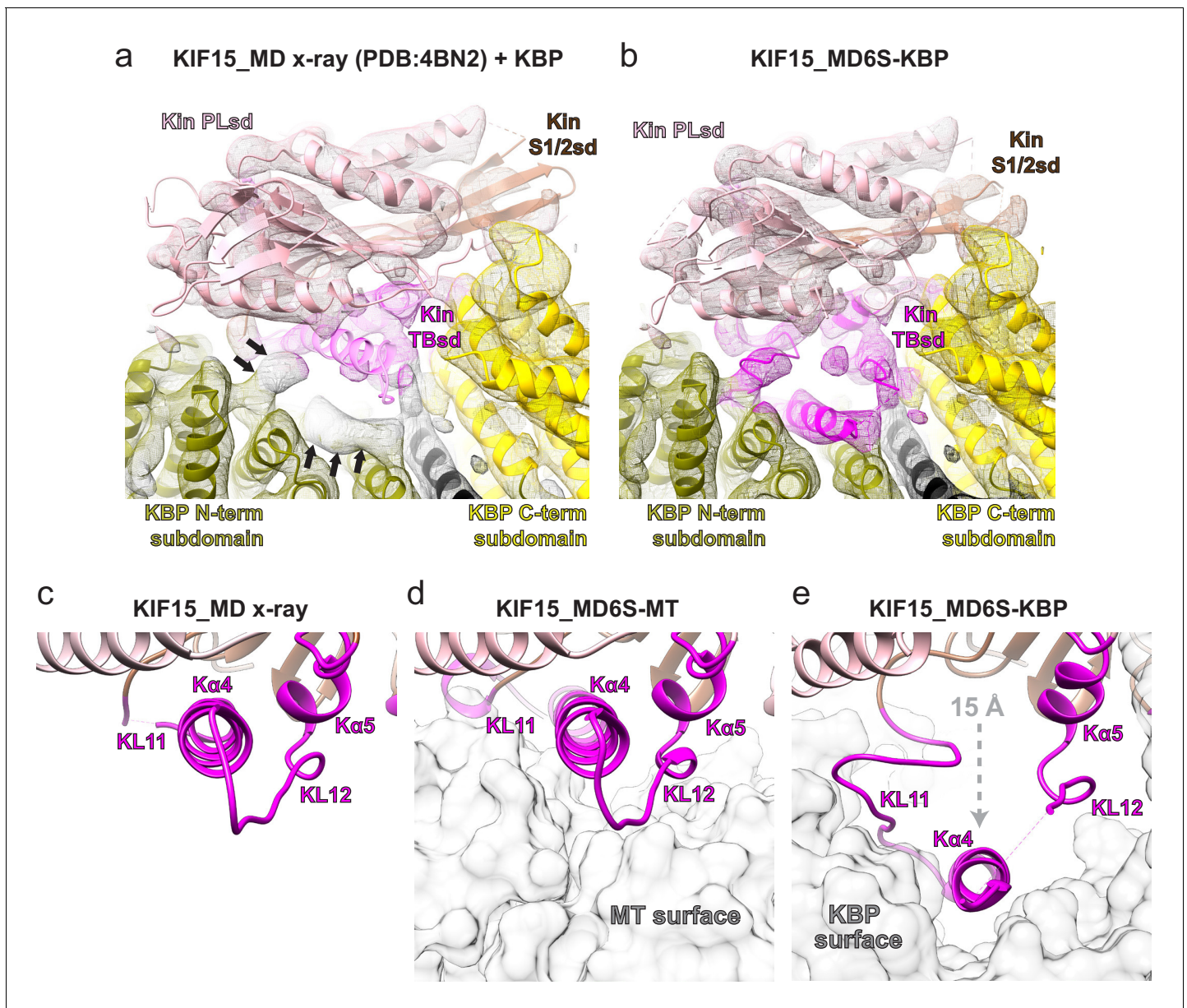


**Figure 3.** The KIF15 motor domain binds kinesin-binding protein (KBP) via rearrangement of its tubulin-binding subdomain. (a) The crystallographic model of the KIF15\_MD alone (PDB: 4BN2 Klejnot *et al.*, 2014) was superimposed on the KIF15 region of the KBP–KIF15\_MD6S complex, with the KIF15 part of the KBP–KIF15\_MD6S complex model hidden. The KIF15\_MD6S Switch 1/2 subdomain (Switch 1/2 subdomain) is coloured sienna, and the P-loop subdomain (Kin-PLsd) is coloured light pink. The TBsd of the KIF15\_MD crystallographic model is shown as pale magenta to illustrate poor fit into density. The KBP subdomains are coloured as labelled. Black arrows indicate unaccounted-for cryo-electron microscopy (cryo-EM) density. Individual secondary structure elements in the tubulin-binding subdomain are labelled. The cryo-EM density for the KBP–KIF15\_MD6S complex is shown in mesh and is coloured by proximity ( $\leq 3.5$  Å) to the fitted model. (b) Same as in panel a, but the whole fitted KBP–KIF15\_MD6S complex model is shown. The KIF15\_MD6S tubulin-binding subdomain (TBsd) is now coloured magenta to indicate good fit into density. (c) Zoomed view of just the TBsd (corresponding to the boxed region in **Figure 3—figure supplement 2d**), showing just the KIF15\_MD-alone crystallographic model. (d) The TBsd in the KIF15\_MD6S-MT model, same view as in panel c. The MT is shown in light grey surface representation. (e) The TBsd in the KBP–KIF15\_MD6S model, same view as in panel c. KBP is shown in light grey surface representation and the  $\sim 15$  Å displacement of helix  $\alpha 4$  is indicated by the dashed grey arrow.

The online version of this article includes the following figure supplement(s) for figure 3:

**Figure supplement 1.** KIF15\_MD6S adopts a canonical MT-bound kinesin conformation.

**Figure supplement 2.** Movement of  $\text{K}\alpha 4$  of the Kin TBsd upon kinesin-binding protein (KBP) binding.

**Figure supplement 3.** Examples of tetratricopeptide repeat (TPR)-containing  $\alpha$ -solenoid proteins binding  $\alpha$ -helical SSE ligands.

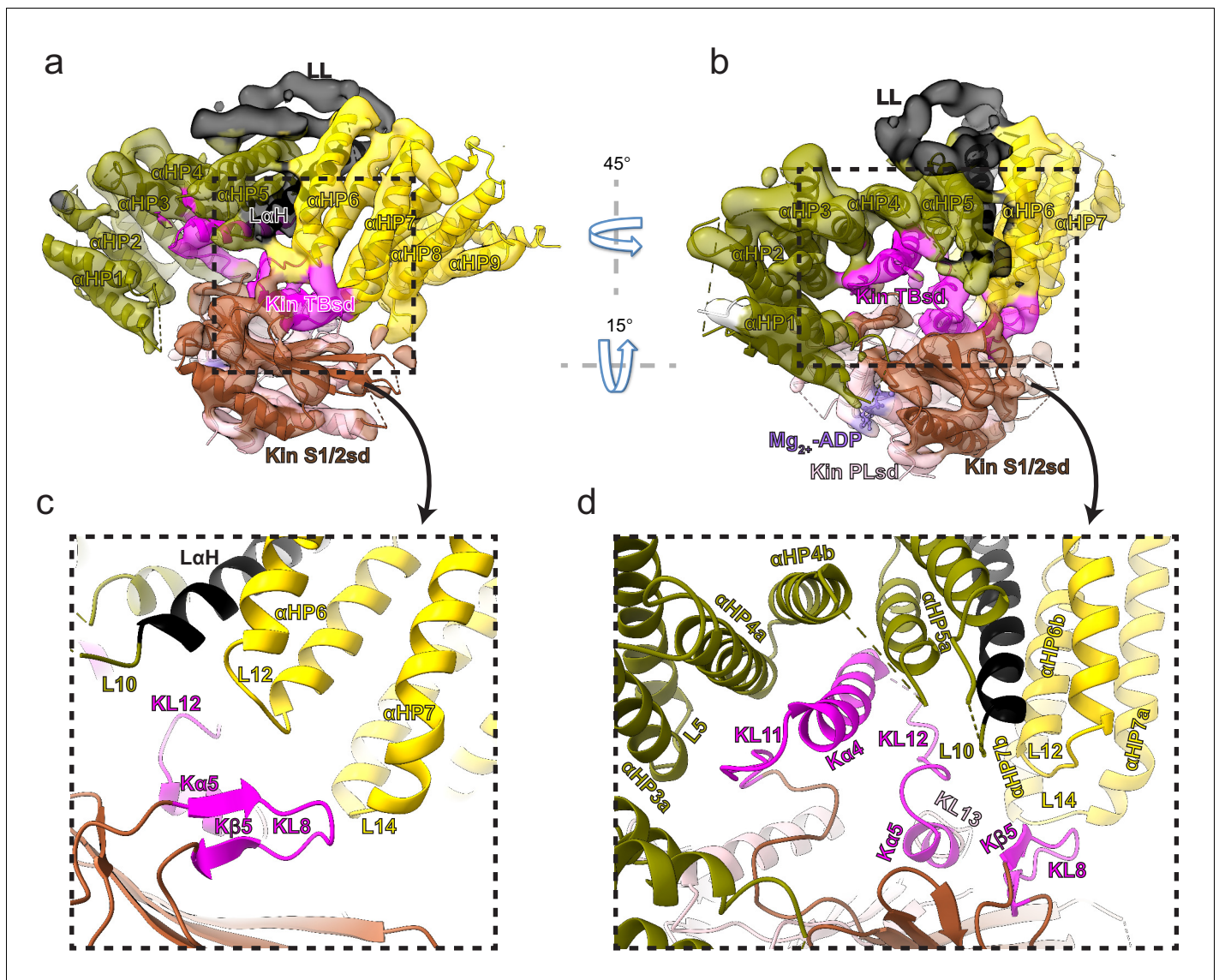


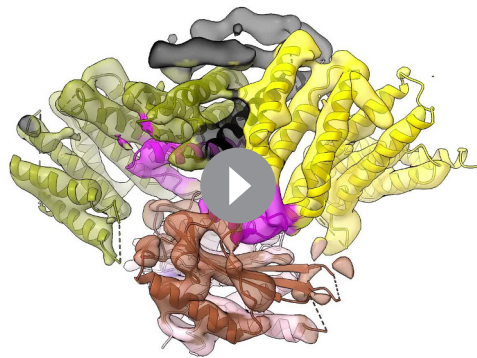
**Figure 4.** Kinesin-binding protein (KBP) binds kinesin MDs via conserved motifs in the  $\alpha$ -solenoid edge loops and  $\alpha$ -helices at the concave face. (a) Pseudo-atomic model of the KBP-KIF15\_MD6S complex (ribbon representation) displayed in cryo-electron microscopy density, using the same viewpoint as **Figure 2a**, but with the KIF15\_MD6S now coloured by subdomain as in **Figure 3**. The KIF15\_MD6S Switch 1/2 subdomain (Kin S1/2 sd) is coloured sienna, and the P-loop subdomain (Kin-PLsd) is coloured light pink. The KIF15\_MD6S tubulin-binding subdomain (TBsd) is coloured magenta. The KBP subdomains are coloured as labelled. The nine helix pairs of KBP are labelled. Semi-transparent density is coloured regionally as per the fitted model and additional density for the linker loop is shown in semi-transparent black. (b) The same as panel a, but rotated 45° and 15° respectively around the axes indicated. (c) Zoomed view of the region indicated in panel a, with density removed and selected KIF15\_MD6S and KBP secondary structure elements labelled. (d) Zoomed view of the region indicated in panel b, with density removed and selected KIF15\_MD6S and KBP secondary structure elements labelled.

The online version of this article includes the following figure supplement(s) for figure 4:

**Figure supplement 1.** Additional kinesin-binding protein (KBP)  $\alpha$ -solenoid edge loops proximal to KIF15\_MD6S.

mutants also had weaker interactions with KIF15\_MDC/KIF1A\_MDC (**Figure 5—figure supplement 2b and c**), again pointing to the additive contributions of loops in the KBP C-terminal subdomain to kinesin binding. Strikingly, mutation of L18 appears to enhance the interaction between KBP and both KIF15\_MDC and KIF1A\_MDC, suggesting that it may somehow contribute to negative regulation of binding in the context of WT KBP.

We then used a previously described inducible peroxisome translocation assay in COS-7 cells (**Kevenaar et al., 2016**). In this assay, dimeric mouse Kif15\_MDC or Kif1A\_MDC constructs with an



**Video 2.** Interaction of kinesin-binding protein (KBP) with the KIF15 motor domain. Model of the KBP–KIF15\_MD6S complex (ribbon representation) displayed in experimental cryo-electron microscopy density. The N-terminal (olive) and C-terminal (gold) subdomains and the linker region (black) are shown in KBP, while the KIF15\_MD6S Switch 1/2 subdomain (Switch 1/2 subdomain) is coloured sienna, the P-loop subdomain (Kin-PLsd) is coloured light pink and the Kif15\_MD tubulin-binding subdomain (TBsd) is coloured magenta. Semi-transparent density is coloured regionally as per the fitted model and additional density for the linker loop is shown in semi-transparent black.

<https://elifesciences.org/articles/61481#video2>

Also, as observed in the pull-down assay, mutation of L1, L3, or L5 had no effect on KBP's inhibition of KIF15\_MDC or KIF1A\_MDC (**Figure 5d–g**). This reinforces the conclusion that while these elements are close enough to form contacts with the parts of the kinesin motor domain in our reconstruction, they do not contribute significantly to KBP inhibition of kinesin-mediated translocation in cells.

Mutation of either of L12 or L14 strongly abrogated KBP inhibition of KIF15\_MDC/KIF1A\_MDC-based translocation, a more pronounced effect than was seen in the pull-down assay. Similarly, although mutation of L10 and L16 had no effect on KBP–kinesin interaction in the pull-down assay, mutation of these loops disrupted KBP inhibition of KIF1A\_MDC and KIF15\_MDC in the translocation assay (**Figure 5d–g**). A subset of the above described mutations was also combined to assess additive effects. Here we observed that KBP constructs containing mutations in both L10 + L12, L10 + L14, or L12 + L14 had similar effects to KBP with only one of the loops mutated (**Figure 5d–g**), suggesting that KBP inhibition is more readily disrupted in the translocation assay.

Interestingly, while all the above described regions affected KBP inhibition of KIF15\_MDC and KIF1A\_MDC equivalently, the L18 KBP mutant inhibited KIF15\_MDC equivalent to wild type, but only exhibited partial inhibition of KIF1A\_MDC-mediated translocation. It should, however, be noted that fewer cells show peroxisome translocation by KIF1A\_MDC when L18 is co-expressed (**Figure 5e**), suggesting that the L18 KBP mutant also inhibits KIF1A\_MDC to some extent. The L18 mutant is the single example of contradictory behaviours between the assays, because it appeared to enhance KBP–kinesin binding in the pull-down assay. Our structural data do not provide a clear rationale for this, and future studies will investigate the role of this region of KBP further and, for

FRB-tag (Kif15\_MDC–FRB or Kif1A\_MDC–FRB) are expressed together with PEX–mRFP–FKBP, a peroxisome-binding construct, along with the various KBP constructs. Addition of rapalog induces FRB–FKBP heterodimerisation and motor-driven peroxisome translocation to the cell periphery, but when the motor is inhibited by KBP, peroxisome translocation is blocked (**Figure 5a–c**). Kinesin-mediated translocation was measured, first by quantifying the number of cells in which peroxisome translocation is seen (**Figure 5d and e**), and second, by quantifying peroxisome intensities above a threshold value in the cell periphery (**Figure 5f and g**). Because of observed differences in peroxisome translocation within the time-frame of rapalog treatment, different peroxisome intensity threshold values and peripheral areas were used for KIF1A and KIF15; this is probably due to differences in motor properties (**Figure 5—figure supplement 3**).

Intriguingly, while the overall trends in perturbation of KBP inhibition by mutagenesis seen in the pull-down assay are recapitulated in the translocation assay, some differences are also observed. As with the pull-down assay, Ala-substitutions in the TPR-containing  $\alpha$ -helices  $\alpha$ HP4a and  $\alpha$ HP4b at the KBP concave face, as well as  $\alpha$ HP5a, all strongly reduced KBP's inhibition of both KIF15\_MDC and KIF1A\_MDC peroxisome translocation activity (**Figure 5d–g**). This can be seen by the extent of peroxisome translocation and in an increase of peroxisomes in the cell periphery after rapalog addition, similar to the control condition without KBP (**Figure 5d–g**).

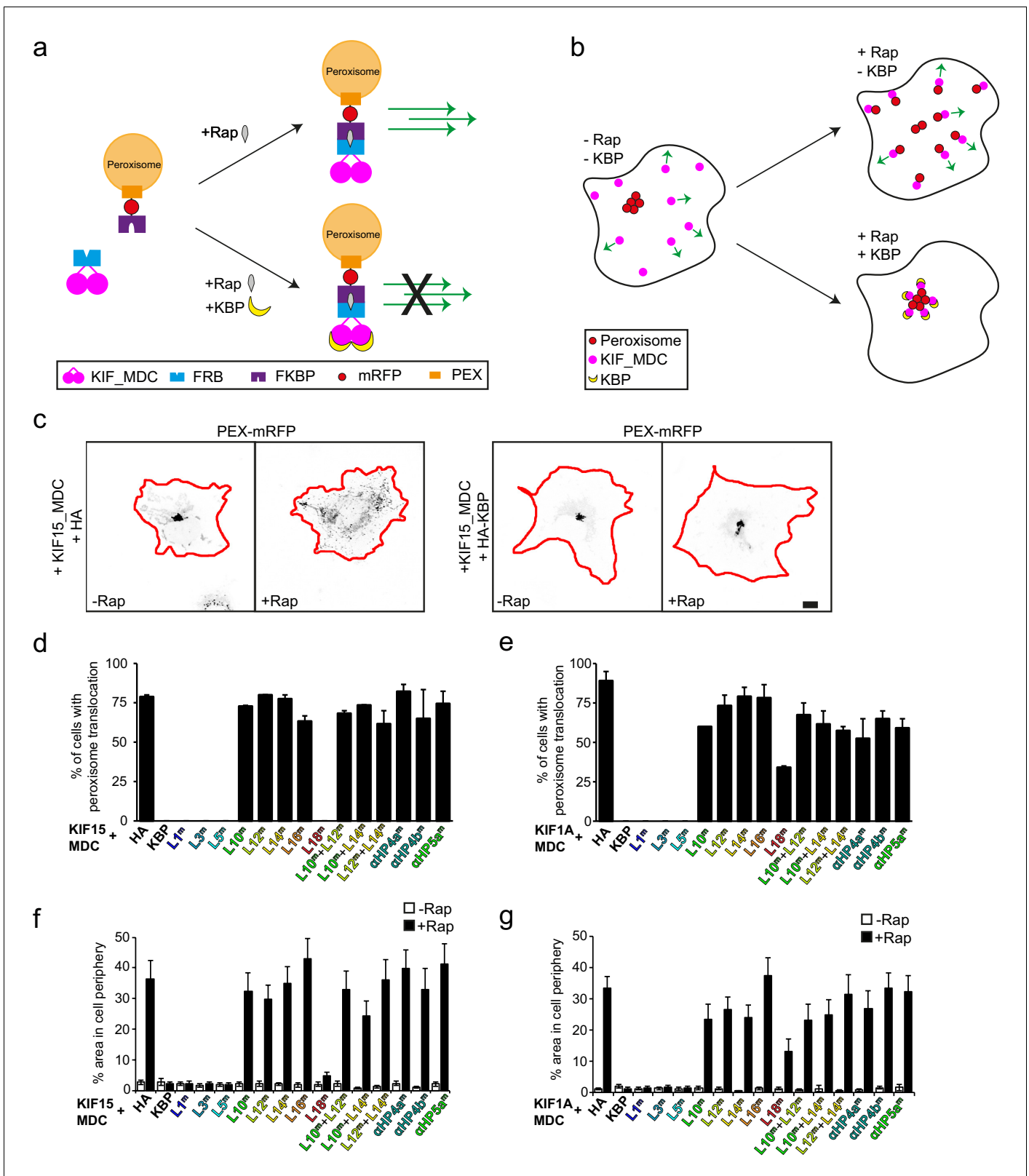


**Figure 5.** Disruption of cryo-electron microscopy defined kinesin-binding protein (KBP)–kinesin interface perturbs KBP inhibition of KIF15- and KIF1A-mediated cargo translocation in cells. (a) Schematic depiction of the inducible peroxisome motility assay, with the kinesin motor domain fused to an FRB domain and PEX fused to an FKBP domain. Addition of rapalog (Rap) links FRB and FKBP and induces peroxisome translocation by kinesin dimers. Expression of KBP inhibits kinesin movement, such that addition of rapalog cannot induce peroxisome translocation. (b) Schematic representation of Figure 5 continued on next page

Figure 5 continued

the inducible peroxisome motility assay in cells. Without rapalog or KBP, peroxisomes localise in the cell centre, whereas kinesin moves towards the cell periphery. Rapalog induces peroxisome translocation into the cell periphery, which is inhibited in the presence of KBP. (c) Representative images of peroxisomes in COS-7 cells expressing KIF15\_MDC-FRB, PEX-mRFP-FKBP, and HA (left panels) or HA-KBP (right panels) without and with addition of rapalog. Scale bar, 10  $\mu\text{m}$ . (d, e) Quantification of the percentage of cells in which peroxisome translocation is observed after rapalog treatment in cells expressing KIF15\_MDC-FRB (d) or KIF1A\_MDC-FRB (e), PEX-mRFP-FKBP, and HA-KBP constructs including the indicated mutants. Data are displayed as mean  $\pm$  s.e.m. ( $n = 28\text{--}35$  cells from two independent experiments). (f, g) Quantification of the area above threshold intensity in the outer 5  $\mu\text{m}$  (KIF1A\_MDC) or 7.5  $\mu\text{m}$  (KIF15\_MDC) of the cell from the total area above threshold intensity in cells expressing KIF15\_MDC-FRB (f) or KIF1A\_MDC-FRB (g), PEX-mRFP-FKBP, and HA-KBP constructs including the indicated mutants without and with rapalog treatment. Data are displayed as mean  $\pm$  s.e.m. ( $n = 28\text{--}35$  cells from two independent experiments).

The online version of this article includes the following figure supplement(s) for figure 5:

**Figure supplement 1.** Kinesin-binding protein (KBP) mutants show similar expression profiles in COS-7 cells.

**Figure supplement 2.** Pull-down experiments demonstrate the effect of kinesin-binding protein (KBP) mutation on the interaction between KIF15 and KIF1A.

**Figure supplement 3.** Kinesin motors show different properties in the peroxisome assay.

example, whether it is subject to post-translational regulation that could regulate KBP's inhibitory activity.

However, taken together, the translocation and pull-down assays both demonstrate the functional importance of the kinesin interaction with the TPR-containing  $\alpha$ -helices at the KBP concave face and the set of loops in the KBP C-terminal subdomain. The translocation and pull-down assays also reveal differences in the sensitivity of the KBP-kinesin interaction to perturbation, where translocation is more readily disrupted than the interactions detected by pull-down. These differences likely reflect the greater complexity of motor regulation during active translocation and could be a function of FRB-FKBP-mediated motor dimerisation. It might also reflect the fact that cellular MTs in the translocation assay can directly compete with KBP for kinesin binding. Overall, these mutation studies support the idea that KBP interacts with different kinesin family members in a similar way via an extended interface at KBP's concave face that is composed of TPR-containing  $\alpha$ -helices and  $\alpha$ -solenoid edge loops, particularly in the C-terminal subdomain.

### Specific sequences in the tubulin-binding subdomain are conserved across KBP-binding kinesin family members

Given that KBP selectively binds and inhibits only a subset of kinesins (Kevenaar et al., 2016), we used our structural data to investigate the basis of this selectivity. Although the resolution of our reconstruction and the flexibility of some loops do not provide a detailed molecular description of the interaction interface, our structure shows that the kinesin tubulin-binding subdomain is the key KBP-interacting region. Analysis of the sequences of this region in KBP-binding and KBP-non-binding kinesins (Figure 6a) revealed patterns of sequence conservation across the entire subdomain in all KBP-binding kinesins; this included both the K $\beta$ 5-KL8 and KL11-K $\alpha$ 4-KL12-K $\alpha$ 5-KL13 regions. In contrast, the equivalent regions are more variable in kinesins that are not inhibited by KBP. The length of KL8, which joins the two K $\beta$ 5 strands, was also consistently five residues long in KBP-binding kinesins, while it was variable in KBP-non-binding kinesins. From our KBP-KIF15\_MD6S structure, the sensitivity of the KBP interaction to KL8 length makes sense considering the tight fit of this loop between KBP L12 and L14 (Figure 6b). In summary, two consensus motifs in KL11-K $\alpha$ 4-KL12-K $\alpha$ 5-KL13 and K $\beta$ 5-KL8 regions of the tubulin-binding subdomain are found in KBP-binding kinesins and these are likely to form the basis of KBP's kinesin family member selectivity. We therefore propose a model where KBP selects and inhibits target kinesins through binding and remodelling a compatible tubulin-binding subdomain, obstructing the kinesin MT-binding surface (Figure 6c).

## Discussion

In this study, we reveal the TPR-containing right-handed  $\alpha$ -solenoid structure of the ~72 kDa KBP using VPP cryo-EM. At the time of writing and to our knowledge, structures of only a few macromolecular complexes <80 kDa have been determined using cryo-EM (Merk et al., 2016; Zhang et al., 2018; Khoshouei et al., 2017; Herzik et al., 2019; Fan et al., 2019). The structure of the KBP-

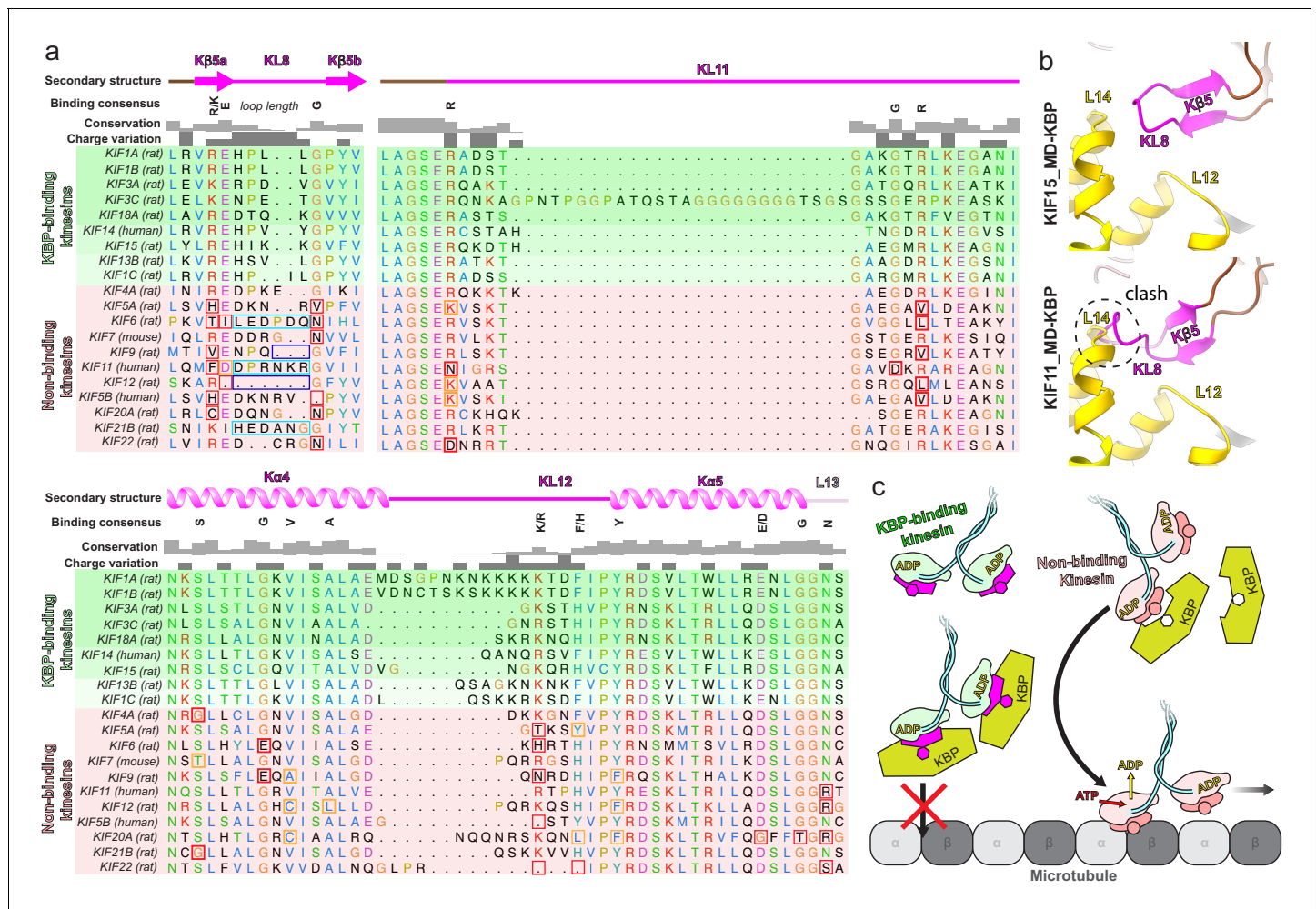


**Figure 6.** Conserved motifs in kinesin-binding protein (KBP)-binding kinesin MDs. (a) Sequence alignment of the tubulin-binding subdomain from kinesin motor domains, made using Clustal Omega multiple sequence alignment (Sievers et al., 2011). Residues are coloured according to standard Clustal X colouring (dependent on residue type and conservation, see [http://bioinfolab.unl.edu/emlab/documents/clustalx\\_doc/clustalx.html#C](http://bioinfolab.unl.edu/emlab/documents/clustalx_doc/clustalx.html#C)). Kinesin MD constructs experimentally assessed for KBP interactivity are taken from Kevenaar et al., 2016; strongest interactors are in rows highlighted in darker shades of green, weaker interactors in lighter shades of green, and non-interactors in red. Secondary structure element, conservation and charge variation columns, as well as a 'binding consensus' column indicating residues/loop length conserved at the interface (according to the KBP-KIF15\_MD6S complex) in KBP-binding but not non-binding kinesins are shown above the alignment. Non-conservation relative to this consensus is shown in boxed sequence; red boxes, non-conservative substitutions, orange boxes, conservative substitutions (general charge/polarity/hydrophobicity retention), cyan boxes, extended loop region, dark blue boxes, truncated loop region. (b) Top panel; view of the Kβ4-KL8 region of the tubulin-binding subdomain in the KBP-KIF15\_MD6S model, coloured as in Figure 4. Bottom panel; as in upper panel, but with the KIF11\_MD cryo-electron microscopy model (PDB: 6TA4 [Peña et al., 2020]) superimposed onto the now hidden KBP-KIF15\_MD6S. Note steric clash introduced by KIF11\_MD's extended KL8. (c) Schematic model of KBP's hypothesized selective kinesin inhibition mechanism. KBP (olive) binds the compatible TBsd of recognised kinesins (magenta) but is incompatible with the TBsd of non-binding kinesins (salmon). For its target kinesins, KBP therefore sterically blocks the TBsd interaction with MTs (grey), preventing activation of kinesin ATP and motility.

KIF15\_MD6S complex shows how KBP binds the KIF15\_MD6S via its concave face and undergoes subtle remodelling of its N-terminal domain to accommodate kinesin binding. This further reinforces the idea that the TPR-containing structures are not simply static scaffolds but can flexibly respond to ligand binding (Pernigo et al., 2018). In contrast, the KIF15 motor domain undergoes a radical conformational change in forming a complex with KBP, in which helix  $\alpha_4$ , the major component of the motor's tubulin-binding subdomain, is displaced from the main MD body by  $\sim 15$  Å into the KBP concave face. This is consistent with previous observations that this region of the kinesin motor domain being rather malleable and able to move independently of the core structure of kinesin motor domains (Wang et al., 2016a; Scarabelli and Grant, 2013). Our evidence suggests this observation

is not due to use of a cysteine-substituted KIF15 motor domain construct because: (i) this protein exhibited equivalent MT-stimulated ATPase activity compared to non-substituted KIF15\_MD (**Figure 2—figure supplement 1a**), (ii) it exhibited structurally canonical MT binding and response to nucleotide (**Figure 3—figure supplement 1**), and (iii) the substituted residues are not well conserved among KBP-binding kinesins (**Figure 6a**). The large displacement of helix  $\alpha 4$  expands the surface area over which the normally compact tubulin-binding subdomain of the kinesin motor domain can interact with KBP, and it is through the sequence and shape of this interface that the selectivity of KBP for a subset of kinesin motors is presumably defined.

Analysis of the KBP–KIF1A\_MD complex (**Figure 2—figure supplement 1c**) supports the idea of a conserved mode of interaction between a subset of kinesins and the concave face of KBP. Interestingly, KIF1A\_MD exhibited flexibility in its interaction with KBP, which was not observed in the KBP–KIF15\_MD6S complex. Whether this reflects a physiological reality, or a result of the EM preparation method is uncertain at present, although we think it unlikely to be due to our use of KIF15\_MD6S. However, our 2D classifications combined with mutation studies strongly suggest KIF15\_MD6S and KIF1A\_MD share an overall similar KBP-binding mode.

Targeted mutations to the various kinesin-binding KBP elements reduced complex affinity, yet no single mutation completely disrupted the interaction in our pull-down assays (**Figure 5—figure supplement 2**). In contrast, in the context of active MT-based cargo translocation in the cellular environment, KBP inhibitory activity appeared more sensitive to disruption (**Figure 5d–g**). Although most KBP mutations that have been reported in GOSHS result in total loss of protein (**Brooks et al., 2005; Dafsari et al., 2015; Valence et al., 2013; Salehpour et al., 2017**), a recent study details missense mutations that only partially reduce protein expression (**MacKenzie et al., 2020**). Our data illustrate that KBP's activity is additionally sensitive to mutations in key regions that affect its ability to bind kinesins.

Our structure shows that KBP binds exclusively to the tubulin-binding subdomain of KIF15\_MD6S, sterically preventing MT attachment. The interaction of kinesin motor domains with the MT surface via its tubulin-binding subdomain stimulates nucleotide exchange and kinesin ATPase activity. In contrast, on interaction with KBP, the displacement of helix  $\alpha 4$  from the kinesin nucleotide-binding site, together with the absence of MT-mediated ordering of KL9 and KL11, means that its catalytic site is distorted and the structural changes associated with MT-stimulated ATPase cannot occur. This could be an important facet of the role of KBP in the energy economy of the cell in addition to directly blocking kinesin–MT interactions.

The concave face of TPR-containing  $\alpha$ -solenoids commonly serve as a recognition platform for specific peptide motifs, including those forming  $\alpha$ -helical structures (**Perez-Riba and Itzhaki, 2019**). Specificity and affinity for target motifs are determined in part by the shape of the  $\alpha$ -solenoid concave face, which in turn is defined by the fold's supertwist. In addition, particular amino acid arrangements at the concave face contribute to partner-binding affinity and specificity, together with additional interfaces formed at the convex surface or  $\alpha$ -solenoid edge (**Zeytuni and Zarivach, 2012**). KBP kinesin specificity and affinity are defined by the interaction of its concave face with the large surface area of the kinesin L11–K $\alpha$ 4–KL12–K $\alpha$ 5–KL13 region, in addition to binding the kinesin K $\beta$ 5–KL8 region at its  $\alpha$ -solenoid edge. Interestingly, distal to the N-terminal MT-binding region of kinesin-1, C-terminally associated kinesin light chain use their unique TPR-containing  $\alpha$ -solenoid concave face to select cargos via recognition of specific peptide motifs (**Cross and Dodding, 2019**). Therefore, peptide selectivity by TPR-containing  $\alpha$ -solenoids is a facet of both kinesin MT-binding and cargo-binding regulatory mechanisms. Such protein–protein interactions may be selectively targeted for disruption (**Randall et al., 2017**), and the insights arising from our work provide future avenues to disrupt KBP–kinesin interactions and thereby explore KBP interactions and regulatory roles.

The effective and selective kinesin inhibitory mechanism of KBP revealed by our work may fulfil specific roles in the kinesin regulatory toolbox employed by cells to spatially and temporarily orchestrate kinesin activity. Future studies will be aimed at understanding how KBP interacts with kinesins in dimeric and/or autoinhibited forms. For example, while KBP does not interact with some target kinesins in autoinhibited conformations (**Malaby et al., 2019**), others that retain a structurally available tubulin-binding subdomain, such as autoinhibited kinesin-3 monomers (**Ren et al., 2018**), are feasible binding partners. KBP can bind to constitutively active dimeric kinesin constructs that lack autoinhibitory regions (**Kevenaar et al., 2016; Malaby et al., 2019**), although the stoichiometry and structural details in this context are unclear. Furthermore, any additional effects of kinesin cargo

binding on their susceptibility to KBP inhibition are not well understood. It will also be of key importance to elucidate the mechanisms of KBP activity regulation, for example, by phosphorylation of KBP and/or kinesins (Kevenaar et al., 2016) and KBP acetylation and targeted degradation by the ubiquitin system (Donato et al., 2017). Our structural characterisation of the KBP–kinesin inhibitory interaction provides an important mechanistic platform from which to expand our understanding of KBP's biological roles in neuronal function and cancer.

## Materials and methods

### Key resources table

Reagent type (species) or resource	Designation	Source or reference	Identifiers	Additional information
Gene ( <i>Homo sapiens</i> )	KIAA1279	GenBank	HGNC:23419	
Gene ( <i>Mus musculus</i> )	KIF1A	GenBank	MGI:108391	
Gene ( <i>Mus musculus</i> )	KIF15	GenBank	MGI:1098258	
Strain, strain background ( <i>Escherichia coli</i> )	BL21(DE3)	NEB	Cat. #: C2527H	Competent cells
Strain, strain background ( <i>Escherichia coli</i> )	BL21-Gold (DE3)	Agilent	Cat. #: 230130	Competent cells
Strain, strain background ( <i>Escherichia coli</i> )	Rosetta2 (DE3)	Novagen	Cat. #: 71400	Competent cells
Cell line ( <i>Homo sapiens</i> )	Human embryonic kidney 239T (HEK293T)	ATCC	CRL-3216 RRID:CVCL_0063	
Cell line ( <i>Cercopithecus aethiops</i> )	<i>Cercopithecus aethiops</i> kidney (COS-7)	ATCC	CRL-1651 RRID:CVCL_0224	
Peptide, recombinant protein	Porcine tubulin (>99% pure)	Cytoskeleton Inc	Cat. #: T240	
Antibody	Anti-HA (mouse monoclonal)	Roche	Cat# 11666606001; RRID:AB_514506	IF (1:500)
Antibody	Anti-mouse IgG1, Alexa488 (goat polyclonal)	Thermo Fisher Scientific	Cat# A-21121, RRID:AB_2535764	IF (1:400)
Antibody	Anti-HA (mouse monoclonal)	Biolegend	Cat# 901533; RRID:AB_2801249	WB (1:2000)
Antibody	Anti-GFP (rabbit polyclonal)	Abcam	Cat# ab290; RRID:AB_303395	WB (1:10000)
Antibody	Anti-rabbit IgG antibody, IRDye 680LT conjugated (goat polyclonal)	LI-COR Biosciences	Cat# 827–11081; RRID:AB_10795015	WB (1:20000)

Continued on next page

Continued

Reagent type (species) or resource	Designation	Source or reference	Identifiers	Additional information
Antibody	Anti-mouse IgG antibody, IRDye 800CW conjugated (goat polyclonal)	LI-COR Biosciences	Cat# 827-08364; RRID:AB_10793856	WB (1:15000)
Recombinant DNA reagent	KBP (plasmid)	<i>Kevenaar et al., 2016</i>		Described in Materials and methods
Recombinant DNA reagent	KIF1A_MD (plasmid)	<i>Atherton et al., 2014</i>		Described in Materials and methods
Recombinant DNA reagent	KIF15_MD (plasmid)	This study		Described in Materials and methods
Recombinant DNA reagent	pebioGFP (plasmid)	<i>van der Vaart et al., 2013</i>	N/A	Described in Materials and methods
Recombinant DNA reagent	BirA coding vector (plasmid)	<i>van der Vaart et al., 2013</i>	N/A	Described in Materials and methods
Recombinant DNA reagent	GW1-PEX3-mRFP-FKBP1 (plasmid)	<i>Kevenaar et al., 2016</i>	N/A	Described in Materials and methods
Recombinant DNA reagent	$\beta$ -actin-Kif1A_MDC-FRB (plasmid)	<i>Kevenaar et al., 2016</i>	N/A	Described in Materials and methods
Recombinant DNA reagent	$\beta$ -actin-Kif15_MDC-FRB (plasmid)	This study	N/A	Described in Materials and methods
Recombinant DNA reagent	pebioGFP-Kif1A_MDC (plasmid)	This study	N/A	Described in Materials and methods
Recombinant DNA reagent	pebioGFP-Kif15_MDC (plasmid)	This study	N/A	Described in Materials and methods
Recombinant DNA reagent	pGW1-HA-KBP (plasmid)	This study	N/A	Described in Materials and methods
Recombinant DNA reagent	pGW1-HA-KBP_L1 (plasmid)	This study	N/A	Described in Materials and methods
Recombinant DNA reagent	pGW1-HA-KBP_L3 (plasmid)	This study	N/A	Described in Materials and methods
Recombinant DNA reagent	pGW1-HA-KBP_L5 (plasmid)	This study	N/A	Described in Materials and methods
Recombinant DNA reagent	pGW1-HA-KBP_L10 (plasmid)	This study	N/A	Described in Materials and methods
Recombinant DNA reagent	pGW1-HA-KBP_L12 (plasmid)	This study	N/A	Described in Materials and methods
Recombinant DNA reagent	pGW1-HA-KBP_L14 (plasmid)	This study	N/A	Described in Materials and methods

Continued on next page

Continued

Reagent type (species) or resource	Designation	Source or reference	Identifiers	Additional information
Recombinant DNA reagent	pGW1–HA–KBP_L16 (plasmid)	This study	N/A	Described in Materials and methods
Recombinant DNA reagent	pGW1–HA–KBP_L18 (plasmid)	This study	N/A	Described in Materials and methods
Recombinant DNA reagent	pGW1–HA–KBP_L10+L12 (plasmid)	This study	N/A	Described in Materials and methods
Recombinant DNA reagent	pGW1–HA–KBP_L10+L14 (plasmid)	This study	N/A	Described in Materials and methods
Recombinant DNA reagent	pGW1–HA–KBP_L12+L14 (plasmid)	This study	N/A	Described in Materials and methods
Recombinant DNA reagent	pGW1–HA–KBP_αHP4a (plasmid)	This study	N/A	Described in Materials and methods
Recombinant DNA reagent	pGW1–HA–KBP_αHP4b (plasmid)	This study	N/A	Described in Materials and methods
Recombinant DNA reagent	pGW1–HA–KBP_αHP5a (plasmid)	This study	N/A	Described in Materials and methods
Sequence-based reagent	KBP_fwd	This study	PCR primer for KBP mutants	TATTATTATGGCGC GCCAGGATCCCCG GAATTCGGCACGA GGGAGGCCGCTAT GGCGAACGTTCC GTGGGCA
Sequence-based reagent	KBP_rev	This study	PCR primer for KBP mutants	CTCGTCGACTCCTAA TCCTTAAGTCA GGCCATCTT
Sequence-based reagent	KBP_L1_fwd	This study	PCR primer for KBP_L1	CTGCATAAAAATCCG GCAGCAGCACCAGCA GCATCCAAATACAGCGCC
Sequence-based reagent	KBP_L1_rev	This study	PCR primer for KBP_L1	GGCGCTGTATTTGGATGC TGCTGGTGCTGCTG CCGGATTTTTATGCAG
Sequence-based reagent	KBP_L3_fwd	This study	PCR primer for KBP_L3	TGAACCACATCGACGC AGGAGGACTGTC GCCGGGGGA
Sequence-based reagent	KBP_L3_rev	This study	PCR primer for KBP_L3	TCCCCCGCCGAC AGTCCTCCTGCG TCGATGTGGTTCA
Sequence-based reagent	KBP_L5_fwd	This study	PCR primer for KBP_L5	ATCTTGTTGGTC TGAAGCAGGAGC AATTGAAACTGCACAG
Sequence-based reagent	KBP_L5_rev	This study	PCR primer for KBP_L5	CTGTGCAGTTTC AATTGCTCCTGC TTCAGACCACAAGAT
Sequence-based reagent	KBP_L10_fwd	This study	PCR primer for KBP_L10	TTTGGTCAAACCTGGA GCAGGAGCAGGAGCA GGAGCAGGACCAGCAG GAGCAGGAGCAGGACCA GGAGGATATCATCAAAGAAA

Continued on next page

Continued

Reagent type (species) or resource	Designation	Source or reference	Identifiers	Additional information
Sequence-based reagent	KBP_L10_rev	This study	PCR primer for KBP_L10	TTTCTTTGATGATATCC TCCTGGTCCTGCTCCT GCTCCTGCTGGTCTCT GCTCCTGCTCCTGCT CCTGCTCCAGTTTGACCAAA
Sequence-based reagent	KBP_L12_fwd	This study	PCR primer for KBP_L12	GAGTTCCTTTCAGATT GGCGGCGCGGTC ACTGACCATATT
Sequence-based reagent	KBP_L12_rev	This study	PCR primer for KBP_L12	AATATGGTCAGTGA CCGCGCCGCCAA TCTGAAAGAACTC
Sequence-based reagent	KBP_L14_fwd	This study	PCR primer for KBP_L14	TAGAGCCCCTAA CTGTAGCAGCA GGACCAGCAGC ATATCTGTTGGTCAAC
Sequence-based reagent	KBP_L14_rev	This study	PCR primer for KBP_L14	GTTGACCAACAGAT ATGCTGCTGGTC CTGCTGCTACA GTTAGGGGCTCTA
Sequence-based reagent	KBP_L16_fwd	This study	PCR primer for KBP_L16	TCCCTGAGAGACC CAGCAGCAGGAG CACCAGCAGGAGC AGGAGCAGGAGC AGCACGCCCTGCCATGTTA
Sequence-based reagent	KBP_L16_rev	This study	PCR primer for KBP_L16	TAACATGGCAGGGC GTGCTGCTCCTGCT CCTGCTCCTGCTGGT GCTCCTGCTGCT GGGTCTCTCAGGGA
Sequence-based reagent	KBP_L18_fwd	This study	PCR primer for KBP_L18	ATTGTTGATTACTG TGCAGCAGGACCA GGAGCCGCCCAGGAAATA
Sequence-based reagent	KBP_L18_rev	This study	PCR primer for KBP_L18	TATTTCTGGGCG GCTCCTGGTCCTGC TGCACAGTAATCAACAAT
Sequence-based reagent	KBP_HP4a_fwd	This study	PCR primer for KBP_L HP4a	ACTCATAACCTATA TGCACTAGCTGCA GTCTACCAGCATCTG
Sequence-based reagent	KBP_L HP4a _rev	This study	PCR primer for KBP_ HP4a	CAGATGCTGGTAG ACTGCAGCTAGT GCATATAGGTTATGAGT
Sequence-based reagent	KBP_HP4b_fwd	This study	PCR primer for KBP_L HP4b	AGTACACTAAAAC GCGCACTTGAGC ACAATGCC
Sequence-based reagent	KBP_L HP4b _rev	This study	PCR primer for KBP_ HP4b	GGCATTGTGCTCA AGTGCGCGTTT TAGTGTACT
Sequence-based reagent	KBP_HP5a_fwd	This study	PCR primer for KBP_L HP5a	GCTATCAATGCTGC TGCGTTGTCAGC GTTTTACATCAATAAG
Sequence-based reagent	KBP_ HP5a _rev	This study	PCR primer for KBP_ HP5a	CTTATTGATGTA ACGCTGACAACGC AGCAGCATTGATAGC
Sequence-based reagent	KIF15_FRB_fwd	This study	PCR primer for KIF15-FRB	AAGCTTGCCACCAT GGCGCGCCTGCCAC CATGGCTCCTGG CTGCAAATCT

Continued on next page

Continued

Reagent type (species) or resource	Designation	Source or reference	Identifiers	Additional information
Sequence-based reagent	KIF15_FRB_rev	This study	PCR primer for KIF15–FRB	AGAGGATTCTAGAAG CAGGCGCGCCAGCG TAGTCTGGGACGTCG TATGGGTAGAATTCTC CTGGTGTCTCAGCTGCCAGA
Sequence-based reagent	bioGFPKIF15_fwd	This study	PCR primer for bioGFPKIF15	AGCTCAAGCTTCGAA TTGGGCGCGCCAGCC ACCATGGCTCCTGG CTGCAAATCT
Sequence-based reagent	bioGFPKIF15_rev	This study	PCR primer for bioGFPKIF15	GAATTCGATATCCTG CAGGTCGACTCCAG ATCCTCATCCTGGT GTCAGCTGCCAGA
Sequence-based reagent	bioGFPKIF1A_fwd	This study	PCR primer for bioGFPKIF1A	TATTATAATGGCGCG CCAGCCACCGCCG GGCCTCTGTGAAGGT
Sequence-based reagent	bioGFPKIF1A_rev	This study	PCR primer for bioGFPKIF1A	CTCGTCGACTCCTC CTCCTCATTTGGG AGAAAACACACCCAA
Commercial assay or kit	EnzChek Phosphate Assay Kit	Invitrogen	E6646	
Chemical compound, drug	AP21967	TaKaRa	Cat# 635057	1 $\mu$ M
Chemical compound, drug	PEI	PolySciences	Cat# 24765–2	
Chemical compound, drug	Fugene	Promega	Cat# E2692	
Software, algorithm	ImageJ	NIH	<a href="https://imagej.nih.gov/ij/">https://imagej.nih.gov/ij/</a> ; RRID:SCR_003070	
Software, algorithm	RELION	<i>Zivanov et al., 2018</i>	n/a	
Software, algorithm	CryoSparc2	<i>Punjani et al., 2017</i>	n/a	
Software, algorithm	CisTEM	<i>Grant et al., 2018</i>	n/a	
Software, algorithm	MiRP	<i>Cook et al., 2020</i>	n/a	Protocol implemented in RELION

## Protein expression and purification for cryo-EM

Full length human KBP residues 1–621 in a PSTCm1 expression vector (with kanamycin resistance and a N-terminal thrombin cleavable 6  $\times$  His-tag) was expressed in Rosetta2 cells (Novagen) as previously described (*Kevenaar et al., 2016*). Following immobilised metal-affinity chromatography with Ni-NTA resin (Qiagen), the 6  $\times$  His-tag was removed via incubation with thrombin protease overnight at 4°C. The protein was then subjected to reverse IMAC and further purified using size exclusion chromatography (SEC) into a buffer of 20 mM Tris-HCl (pH 7.4), 150 mM NaCl, 2.5 mM CaCl<sub>2</sub>, and 1 mM DTT. Protein was snap-frozen and stored in at –80°C.

A human KIF15 motor domain and neck linker construct (residues 1–375) in a pET21a vector with a C-terminal 6  $\times$  His-tag was generated by chemical synthesis (GenScript, Piscataway, NJ). Six of the eight cysteine residues (C5S, C50S, C162S, C294S, C314S, and C346S) were mutated and two

cysteines were inserted (S250C and G375C) for orthogonal experiments not described further here. We refer to this construct as KIF15\_MD6S. KIF15\_MD6S was expressed and purified using methods previously described (*Rosenfeld et al., 2005*), then buffer exchanged into 25 mM HEPES pH 7.5, 100 mM KCl, 2 mM MgCl<sub>2</sub>, 1 mM EGTA, 1 mM DTT, 0.1 mM ATP, snap frozen in liquid nitrogen, and stored at –80°C.

A human KIF1A motor domain and neck linker construct (KIF1A\_MD residues 1–362) in a pFN18a vector (with a TEV protease-cleavable N-terminal Halo-tag and a C-terminal 6 × His-tag) was expressed in BL21-Gold (DE3) cells, as previously described (*Atherton et al., 2014*). Following a first IMAC with Ni-NTA resin, the Halo-tag was removed via incubation overnight with TEV protease at 4°C. The protein was then isolated from TEV via a second IMAC with Ni-NTA resin and further purified by SEC into a storage buffer of (20 mM HEPES, pH 7, 150 mM NaCl, 5 mM MgCl<sub>2</sub>, 0.1 mM ADP, and 1 mM TCEP).

KIF15\_MD6S or KIF1A\_MD complexes with KBP were purified via IMAC using the 6 × His-tag on the kinesin constructs. Briefly, His-tagged kinesins were incubated with a 10 times excess of KBP in 20 mM Tris-HCl (pH 7.5), 150 mM NaCl, 1 mM MgCl<sub>2</sub>, 10 mM Imidazole, 1 mM DTT, and 0.2 mM ADP for 5 min at 4°C. Following IMAC, complexes were eluted from the Ni-NTA resin (Qiagen) by addition of 200 mM imidazole, then dialysed at 4°C for 4 hr into 20 mM Tris-HCl (pH 7.5), 150 mM NaCl, 1 mM MgCl<sub>2</sub>, 1 mM DTT, and 0.2 mM ADP.

### Steady-state ATPase assay

ATPase activity of KIF15\_MD6S was measured in ATPase buffer (50 mM potassium acetate, 25 mM HEPES, 5 mM magnesium acetate, and 1 mM EGTA, pH 7.50) by measuring phosphate production in the presence of a minimum of a fivefold molar excess of paclitaxel-stabilised MTs, using a commercially available kit (EnzChek, Molecular Probes) at 20°C.

### Sample preparation for cryo-EM

KBP was prepared for cryo-EM using three different approaches. In the first approach, KBP was diluted to 0.15 mg/ml in KBP dilution buffer (20 mM Tris-HCl, pH 7.5, 150 mM NaCl, and 2 mM DTT) and 4 µl were applied to glow-discharged C-flat 2/2 holey carbon EM grids (Protochips, Morrisville, NC). For the second approach, KBP was diluted to 0.3 mg/ml in KBP dilution buffer and 4 µl were applied to glow-discharged 1.2/1.3 AuFoil gold grids (Quantifoil). For the third approach, glow-discharged C-flat 2/2 holey carbon EM grids were coated with graphene-oxide (GO) according to the protocol described by Cheng and colleagues (*Cheng et al., 2020*) and then 4 µl of KBP diluted to 0.02 mg/ml in KBP dilution buffer were added.

Kinesin motor domain–KBP complexes were diluted to 0.03 mg/ml in KBP–kinesin dilution buffer (20 mM Tris-HCl [pH 7.5], 50 mM NaCl, 1 mM MgCl<sub>2</sub>, 1 mM DTT, and 0.2 mM ADP) and 4 µl were added to the GO-coated gold grids described above. After a 30 s incubation of samples on the EM grid in a Vitrobot Mark IV (FEI Co., Hillsboro, OR) set at 4°C and 80% humidity, samples were blotted (6–8 s, blot force –10) and vitrified in liquid ethane. All steps were performed at 4°C.

For preparation of the KIF15\_MD6S-MT complex, porcine tubulin (>99% pure, Cytoskeleton Inc) was polymerised in MES polymerisation buffer (100 mM MES, 1 mM MgCl<sub>2</sub>, 1 mM EGTA, and 1 mM DTT, pH 6.5) with 5 mM GTP at 37°C and then stabilised with 1 mM paclitaxel. Approximately 70 µM KIF15\_MD6S was pre-incubated for 5 min with 5 mM of AMPPNP in BRB80 at room temperature, and then mixed with 20 µM stabilised MTs. After a further incubation of 15 min, a 4 µl droplet was applied to a pre-glow discharged holey carbon grid (2/2 C-flat, Protochips Inc), blotted for 3.5 s, and then vitrified in liquid ethane using a Vitrobot Mark IV at ambient temperature and 80% humidity.

### Cryo-EM data collection

For dataset of KBP alone or KBP–KIF15\_MD6S, low-dose movies were collected automatically using EPU software (Thermo Fisher, MA, USA) on a Titan Krios electron microscope (Thermo Fisher) operating at 300 kV, with a K2 summit direct electron detector (Gatan, CA, USA) and a quantum post-column energy filter (Gatan) operated in zero-loss imaging mode.

Datasets of KBP alone were collected either at eBIC or the ISMB, Birkbeck using a VPP, a sampling of  $\sim 1.05$  Å/pixel and a nominal defocus range of 0.5–0.7  $\mu\text{m}$ . The total dose was 42 e-/Å<sup>2</sup> over 40 frames, with the detector operating in counting mode at a rate of  $\sim 5$  e-/pixel/s.

Datasets of KBP–kinesin complexes were collected at the ISMB, Birkbeck without a phase plate and a nominal defocus range of 1.5–4  $\mu\text{m}$ . KIF1A\_MD–KBP complexes were collected at a sampling of 0.85 Å/pixel, whereas KBP–KIF15\_MD6S complexes were collected at a sampling of 1.047 Å/pixel. For KIF1A\_MD–KBP complexes, the total dose was 88 e-/Å<sup>2</sup> over 36 frames, with the detector operating in counting mode at a rate of 7.1 e-/pixel/s. For KBP–KIF15\_MD6S complexes, the total dose was 80 e-/Å<sup>2</sup> over 64 frames, with the detector operating in counting mode at a rate of 5.7 e-/pixel/s.

The KIF15\_MD6S-MT dataset was collected manually on a Tecnai Polara microscope (Thermo Fisher) at the ISMB, Birkbeck, operating at 300 kV, with a K2 summit direct electron detector (Gatan, CA, USA) and a quantum post-column energy filter (Gatan) operated in zero-loss imaging mode. A nominal defocus range of 1.0–3.5  $\mu\text{m}$  and a final pixel size of 1.39 Å was used. The total dose was 32 e-/Å<sup>2</sup> over 50 frames, with the detector operating in counting mode at a rate of 6.2 e-/pixel/s.

### Cryo-EM data processing

Low-dose movies were motion-corrected using MotionCor2 (Zheng *et al.*, 2017) with a patch size of 5, generating full-dose and dose-weighted sums. CTF determination was performed on full-dose sums with gCTF (Zhang, 2016) and then dose-weighted sums were used for all further processing. Data were cleaned at this stage by first excluding all micrographs with gCTF resolutions worse than 4.5 Å, as estimated with a custom cross-correlation coefficient cutoff (Python script kindly shared by Radostin Danev), then manually removing micrographs with poor appearance (ice contamination, protein aggregation, or poor GO coverage) in real or reciprocal space. For KBP alone data, micrographs with calculated phase shifts outside the expected phase shift progression at each plate position were also excluded.

Particles were first picked using Eman2's neural network picker (Bell *et al.*, 2018), with a 180 pixel box size for KBP-alone and KBP–KIF15\_MD6S datasets, or a 220 pixel box size for the KBP–KIF1A\_MD datasets. Good 2D classes were then used as templates to pick the data with Gautomatch (<http://www.mrc-lmb.cam.ac.uk/kzhang/>).

For Eman2 neural network picker or Gautomatch-derived particles from each dataset, separate multiple rounds of 2D classification were performed in RELION v3.0 (Zivanov *et al.*, 2018), cryoSPARC2 (Punjani *et al.*, 2017), or cisTEM (Grant *et al.*, 2018). This resulted in a total of six sets of good 2D classes showing clear secondary structure for each dataset, two produced by each programme for each picking method. For each dataset, these six good 2D class sets for each dataset were then combined and duplicate particles removed. At this stage, for each sample (KBP-alone, KBP–KIF15\_MD6S, or KBP–KIF1A\_MD) good 2D classes from their constituent datasets were combined.

KBP–KIF15\_MD6S or KBP–KIF1A\_MD datasets composed of their respective constituent datasets were easily combined, being from the same microscope and optical set up. However, KBP-alone data were collected on different microscopes and had a range of pixel sizes (<2% difference). KBP-alone data therefore was combined at this stage using the optics grouping protocol in RELION v3.1 (Zivanov *et al.*, 2018).

KBP-alone and KBP–KIF15\_MD6S data were taken to 3D processing at this stage, while multiple attempts to process KBP–KIF1A\_MD data in 3D gave no reliable results. For KBP-alone and KBP–KIF15\_MD6S data, de novo initial 3D models were created in cryoSPARC2. For KBP–KIF15\_MD6S data, a single round of 3D classification was performed in RELION v3.0 and the best class selected and auto-refined. For KBP-alone data, 3D classification in RELION v3.1 or cryoSPARC2 did not reveal different 3D structures or improve reconstructions over sorting only in 2D; therefore, particles selected with 2D classification were used as direct input for auto-refinement. The final KBP-alone map was sharpened with a B-factor of  $-200$  to the gold-standard Fourier shell correlation (FSC) 0.143 cutoff (4.6 Å). The KBP–KIF15\_MD6S map was sharpened locally with a B-factor of  $-495$ , according to local resolutions determined using RELION v3.1's inbuilt local resolution software.

The KIF15\_MD6S-MT dataset was processed using our MT RELION-based pipeline (MiRP) as described previously, using low-pass filtered KIF5B\_MD-decorated MTs as references (Atherton *et al.*, 2019; Cook *et al.*, 2020). KIF15\_MD6S 13-protofilament-MTs were the most

common MT architecture and were selected after supervised 3D classification in MiRP for analysis. The symmetrised asymmetric unit (KIF15\_MD6S plus a tubulin dimer) was locally sharpened in UCSF Chimera with a B-factor of  $-134$  according to local resolutions determined using RELION v3.0's inbuilt local resolution software.

All displayed 3D molecular representations were made in UCSF Chimera or ChimeraX software (Pettersen *et al.*, 2004; Goddard *et al.*, 2018). Data collection and model refinement statistics can be found in Table 1.

## Cryo-EM model building and refinement

Due to low overall homology to available structures in the protein data bank (PDB), structure prediction of KBP produced poor models with little resemblance to the cryo-EM density. KBP was therefore modelled using a combination of secondary structure prediction, TPR prediction, fragment homology information, prior knowledge of right-handed alpha-solenoid proteins, and with reference to the cryo-EM density.

TPR motifs were identified in the KBP sequence using the TPRpred server (Karpenahalli *et al.*, 2007) available in the MPI Bioinformatics Toolkit (Zimmermann *et al.*, 2018). Secondary structure predictions using Raptor X (Wang *et al.*, 2016b), iTasser (Roy *et al.*, 2010), JPred (Drozdetskiy *et al.*, 2015), Spider2 (Yang *et al.*, 2017), PSSpred (Yan *et al.*, 2013), and SOPMA (Geourjon and Deléage, 1995) were then run on the sequence and consensus between these multiple predictions used to assign likely  $\alpha$ -helical content. To identify regions dispensable for the overall fold and likely disordered loop regions, disorder prediction was performed with Raptor X and inter-species low homology regions in KBP (from early Metazoans to humans) were determined via Clustal Omega multiple sequence alignment (Sievers *et al.*, 2011). Finally, weak homology models for overlapping fragments of the structure were identified using the HHpred (Hildebrand *et al.*, 2009) server in the MPI Bioinformatics Toolkit.

With the information described above a sequence alignment was built with KBP and the following fragment homology model PDBs; 5OJ8, 4A1S, 3QC1, 4NQ0, 4AIF, and 5M  $\times$  5. This sequence alignment was used as a basis for multiple rounds of modelling and flexible fitting with Modeller (Sali and Blundell, 1993) and Flex-EM (Topf *et al.*, 2008) respectively, using  $\alpha$ -helical secondary structure restraints. This modelling process was guided by consistency with the cryo-EM density and secondary structure and TPR predictions described above. Finally, the structure was refined against the cryo-EM density in real-space with five macro-cycles in Phenix (Afonine *et al.*, 2018). All 19 predicted and modelled helices were accounted for by rod-like cryo-EM density in the reconstruction and at 4.6 Å resolution, density was discernible for bulky side chains in the TPR regions (Figure 1—figure supplement 1a and b), providing a validation of the assigned sequence directionality in the fold.

The KBP–KIF15\_MD6S model was built as follows: the final KBP model described above and the KIF15\_MD X-ray crystallographic model (PDB code:4BN2 Klejnot *et al.*, 2014) were rigid fitted into the KBP–KIF15\_MD6S density in Chimera. Density for an extended  $\alpha 6$ -helix and docked neck-linker in KIF15\_MD6S were absent; therefore, Modeller was used to model a short  $\alpha 6$ -helix and the neck-linker removed. A model for the L11,  $\alpha 4$ -helix, and L12 region in KIF15\_MD6S were then created using Coot (Emsley and Cowtan, 2004) and Modeller. The model was refined into the cryo-EM density in real-space using Phenix (Afonine *et al.*, 2018) with secondary structure restraints. A first refinement of 15 cycles used rigid bodies describing  $\alpha$ -helical hairpins in KBP to get a good rough fit. Following this, the whole complex was further refined without rigid bodies for another five macro-cycles.

The KIF15\_MD6S–MT model was built as follows: the KIF15\_MD, KIF11\_MD, and KIF5B\_MD-tubulin X-ray crystallographic models (PDB codes:4BN2 Klejnot *et al.*, 2014; Gigant *et al.*, 2013; Parke *et al.*, 2010) were used as homology models in Modeller to build the KIF15 part of the complex. The KIF15\_MD6S model and the paclitaxel–MT tubulin dimer model (Kellogg *et al.*, 2017) were then rigid fitted into KIF15\_MD6S–MT density, combined then refined in real-space with five macro-cycles in Phenix with peptide backbone restraints.

## Antibodies, reagents, and expression constructs for cell biology

The following antibodies were used for immunofluorescence staining: mouse anti-HA (1:500, Roche) and goat-anti-mouse Alexa 488 (1:400, Thermo Fisher Scientific). The following antibodies were used for western blot: mouse anti-HA (1:2,000, BioLegend), rabbit anti-GFP (1:10,000, Abcam), goat anti-mouse IRDye800CW (1:15,000, LI-COR), and goat-anti-rabbit IRDye680LT (1:20,000, LI-COR). A reagent used in this study is rapalog (AP21967, TaKaRa).

The following DNA expression constructs in this study have been described before: GW1-PEX3-mRFP-FKBP1,  $\beta$ -actin-Kif1A\_MDC-FRB (Kevenaar *et al.*, 2016) (mouse cDNA), BirA coding vector (van der Vaart *et al.*, 2013), and pebioGFP (van der Vaart *et al.*, 2013). pGW1-HA-KBP contained a linker (GGATCCCCGGAATTCGGCACGAGGGAGGCCGCT) between the HA tag and KBP and was cloned using PCR-based strategies with human KBP cDNA (KIAA1279, IMAGE clone 4550085) as template and ligation into the pGW1-HA backbone. A similar strategy was used to generate the mutated KBP constructs, listed in Table 2.  $\beta$ -actin-KIF15\_MDC-FRB was cloned using a PCR-based Gibson Assembly strategy with mouse KIF15 cDNA as template into the  $\beta$ -actin-KIF1A\_MDC-FRB backbone. PebioGFP-KIF1A\_MDC and pebioGFP-KIF15\_MDC were cloned into the pebioGFP backbone using PCR-based strategies with MDC-FRB constructs as templates.

## Cell culture, transfection, and immunofluorescence staining

COS-7 cells were purchased from ATCC and routinely checked for mycoplasma contamination using LT07-518 Mycoalert assay (Lonza). Cells were cultured in 50/50 DMEM (Lonza)/Ham's F10 (Lonza) medium supplemented with 10% FCS (Sigma) and 1% penicillin/streptomycin (Sigma). One day before transfection cells were diluted and plated on 18 mm glass coverslips. COS-7 cells were transfected using FuGENE6 (Roche) following the manufacturer's protocol. Next day, rapalog (final concentration 1  $\mu$ M) was added and cells were incubated for 3 hr. Cells were then fixed with 4% formaldehyde/4% sucrose in phosphate-buffered saline (PBS) for 10 min at room temperature, washed three times PBS-CM (PBS supplemented with 1 mM MgCl<sub>2</sub> and 0.1 mM CaCl<sub>2</sub>), permeabilised in 0.2% TritonX-100 for 15 min, and washed one time with PBS-CM. Cells were first incubated with 0.2% gelatin for 30 min at 37°C, and then with primary antibodies, diluted in 0.2% gelatin, for 30 min at 37°C. After washing three times with PBS-CM, cells were incubated for 30 min at 37°C with secondary antibody diluted in 0.2% gelatin, washed three times in PBS-CM, and finally mounted using Fluoromount (Invitrogen).

**Table 2.** Kinesin-binding protein (KBP) mutants used in this study.

The original and mutated amino acid (top) and nucleotide sequences (bottom) are shown for each construct.

Construct	Original sequence	Mutated to
L1	EKEPYK gagaaggaaccatacaag	AAAPAA gcagcagcaccagcagca
L3	TEE acggaggag	AGG gcaggagga
L5	REE agagaagaa	AGA gcaggagca
L10	KISATEDTPEAEGEVPEL aagatctcagccacagaagacactc ctgaagctgaaggagaagtgcagagctt	AGAGAGAGPAGAGAGPGG gcaggagcaggagcaggagca ggaccagcaggagcaggagcaggaccaggagga
L12	DGY gatggttat	GGA ggcggcgcg
L14	DLNPQY gacctgaatccacagtat	AAGPAA gcagcaggaccagcagca
L16	NKVFPEHIGEDVL aataaagtattccctgagcata taggggaagatgttctt	AAGAPAGAGAGAA gcagcaggagcaccagcag gagcaggagcaggagcagca
L18	EKHPE gaaaagcatcctgag	AAGPG gcagcaggaccagga
$\alpha$ HP4a	YLAQ tacctagctcaa	ALAA gcactagctgca
$\alpha$ HP4b	Q cag	A gca
$\alpha$ HP5a	TLSQ acctgtgcacag	ALSA gcgtgtgcagc

## Cell biology image analysis and quantification

Fixed cells were imaged on a Carl Zeiss LSM 700 confocal laser scanning microscope running ZEN2011 software, using a Plan-Apochromat 40×/1.30 oil DIC objective and image settings were maintained the same for all images within one experiment. Images were acquired of cells that express similar levels of HA-KBP constructs based on immunostaining (**Figure 5—figure supplement 1**). Cells were selected on a first come first served basis. Images were processed and analysed using Fiji software (*Schindelin et al., 2012*). To calculate the percentage of cells in which translocation of peroxisomes was observed, imaged cells were classified as either translocating, when peroxisomes re-localised into the cell periphery, or not translocating, when peroxisomes remained in the cell centre. For quantification of PEX translocation, an ROI of the cell area was drawn and from this a second ROI at 5 (KIF1A\_MDC) or 7.5 (KIF15\_MDC)  $\mu\text{m}$  from the outer cell area was created. Images were thresholded at 7500 (KIF15\_MDC) or 10,000 (KIF1A\_MDC). Different peripheral areas and threshold values were defined for the two kinesins, due to observed differences in translocation properties between the kinesins (compare **Figure 5—figure supplement 3a–c**). For the two selected ROIs, the area with fluorescent intensity above threshold was determined in the RFP channel. From these values the percentage of cell area above threshold in the cell periphery from the total area above threshold was calculated.

## Pull-down experiments and western blotting

HEK293T cells were purchased from ATCC and routinely checked for mycoplasma contamination using LT07-518 Mycoalert assay (Lonza). Cells were cultured in 50/50 DMEM (Lonza)/Ham's F10 (Lonza) medium supplemented with 10% FCS (Sigma) and 1% penicillin/streptomycin (Sigma). One day before transfection cells were diluted and plated into 6-well plates. Cells were co-transfected with pCl-Neo-BirA, HA-tagged constructs, and bioGFP-tagged constructs using MaxPEI (Polysciences) in a ratio of 3/1 PEI/DNA, according to the manufacturer's protocol. After 24 hr of expression, cells were washed in ice-cold PBS and lysed in lysis buffer (100 mM Tris-HCl pH 7.5, 150 mM NaCl, 1% Triton X-100, and protease inhibitors [Roche]) for 30 min on ice. Lysates were cleared by 30 min centrifugation at 13.2 krpm at 4°C and supernatants were incubated with blocked (incubation for 30 min at RT in 50 mM Tris-HCl pH 7.5, 150 mM KCl, and 0.2  $\mu\text{g}/\mu\text{l}$  chicken egg albumin) Streptavidin Dynabeads M-280 (Invitrogen) for 1.5 hr at 4°C. Beads were then washed five times with washing buffer (100 mM Tris-HCl pH 7.5, 250 mM NaCl, and 0.5% Triton X-100) and proteins were eluted from the beads by boiling for 10 min at 95°C in 2× DTT+sample buffer (20% glycerol, 4% SDS, 200 mM DTT, 100 mM Tris-HCl pH 6.8, and bromophenol blue).

Protein samples were run on 10% SDS-PAGE gels and transferred to nitrocellulose membranes (Bio-Rad) by semi-dry blotting at 16V for 1 hr. Membranes were blocked by incubation in 3% bovine serum albumin (BSA) in PBST (PBS supplemented with 0.02% Tween20) for 1 hr at room temperature. This was followed by overnight incubation with primary antibodies in 3% BSA-PBST. Membranes were washed three times with PBST, incubated with secondary antibody in 3% BSA-PBST for 1 hr at room temperature, and washed three times with PBST. Membranes were scanned using an Odyssey Infrared Imaging system (LI-COR Biosciences) and blots were acquired at 680 nm and 800 nm.

## Acknowledgements

JA was supported by a grant from the Medical Research Council (MRC), UK (MR/R000352/1) to CAM, and JL and AP were supported by a grant from Worldwide Cancer Research, UK (16–0037) awarded to JL and CAM. We thank Dr Alexander Cook for technical and processing assistance at the ISMB and Dr Radostin Danev at the Graduate School of Medicine, The University of Tokyo for custom processing scripts. Cryo-EM data collected at the Institute of Structural and Molecular Biology (ISMB), Birkbeck was on equipment funded by the Wellcome Trust, UK (202679/Z/16/Z, 206166/Z/17/Z and 079605/Z/06/Z) and the Biotechnology and Biological Sciences Research Council (BBSRC), UK (BB/L014211/1). We thank Dr Natasha Lukoyanova for support during data collection at the ISMB. For the remaining EM data collection, we acknowledge Diamond for access and support to the Electron Bioimaging Centre (eBIC) at Diamond, Harwell, UK, funded by the MRC, BBSRC and Wellcome Trust, UK. SSR was supported by a grant from the National Institute of General Medical

Sciences (R01GM130556). NO and MOS were supported by a grant awarded to MOS from the Swiss National Science Foundation (31003A\_166608). JJA was supported by the Netherlands Organization for Scientific Research (NWO-ALW-VICI, CCH) and the European Research Council (ERC) (ERC-consolidator, CCH).

## Additional information

### Funding

Funder	Grant reference number	Author
Medical Research Council	MR/R000352/1	Joseph Atherton Carolyn A Moores
Worldwide Cancer Research	16-0037	Julia Locke Alejandro Peña Carolyn A Moores
Wellcome Trust	202679/Z/16/Z	Carolyn A Moores
Biotechnology and Biological Sciences Research Council	BB/L014211/1	Carolyn A Moores
National Institute of General Medical Sciences	R01GM130556	Steven S Rosenfeld
Swiss National Science Foundation	31003A_166608	Natacha Olieric Michel O Steinmetz
Netherlands Organization for Scientific Research	NWO-ALW-VICI	Jessica JA Hummel Casper C Hoogenraad
European Research Council	ERC-consolidator	Jessica JA Hummel Casper C Hoogenraad
Wellcome Trust	206166/Z/17/Z	Carolyn A Moores
Wellcome Trust	079605/Z/06/Z	Carolyn A Moores
Netherlands Organization for Scientific Research	CCH	Jessica JA Hummel Casper C Hoogenraad
European Research Council	CCH	Jessica JA Hummel Casper C Hoogenraad

The funders had no role in study design, data collection and interpretation, or the decision to submit the work for publication.

### Author contributions

Joseph Atherton, Conceptualization, Resources, Data curation, Formal analysis, Validation, Investigation, Visualization, Methodology, Writing - original draft, Project administration, Writing - review and editing, Corresponding author; Jessica JA Hummel, Conceptualization, Resources, Data curation, Formal analysis, Validation, Investigation, Visualization, Methodology, Writing - original draft, Writing - review and editing; Natacha Olieric, Conceptualization, Resources, Writing - review and editing; Julia Locke, Alejandro Peña, Resources, Investigation, Writing - review and editing; Steven S Rosenfeld, Michel O Steinmetz, Resources, Funding acquisition, Writing - review and editing; Casper C Hoogenraad, Conceptualization, Resources, Supervision, Funding acquisition, Project administration, Writing - review and editing; Carolyn A Moores, Conceptualization, Resources, Supervision, Funding acquisition, Visualization, Writing - original draft, Project administration, Writing - review and editing

### Author ORCIDs

Joseph Atherton  <https://orcid.org/0000-0002-6362-2347>

Casper C Hoogenraad  <http://orcid.org/0000-0002-2666-0758>

Carolyn A Moores  <http://orcid.org/0000-0001-5686-6290>

### Decision letter and Author response

Decision letter <https://doi.org/10.7554/eLife.61481.sa1>

Author response <https://doi.org/10.7554/eLife.61481.sa2>

## Additional files

### Supplementary files

- Transparent reporting form

### Data availability

Cryo-EM electron density maps and models have been deposited in the electron microscopy data bank (EMDB) and the protein data bank (PDB), respectively. The relevant deposition codes are provided in Table 1.

The following datasets were generated:

Author(s)	Year	Dataset title	Dataset URL	Database and Identifier
Atherton J, Hummel JJA, Olieric N, Locke J, Peña A, Rosenfeld SS, Steinmetz MO, Hoogenraad CC, Moores CA	2020	Kinesin binding protein (KBP)	<a href="http://www.rcsb.org/structure/6ZPG">http://www.rcsb.org/structure/6ZPG</a>	RCSB Protein Data Bank, 6ZPG
Atherton J, Hummel JJA, Olieric N, Locke J, Peña A, Rosenfeld SS, Steinmetz MO, Hoogenraad CC, Moores CA	2020	Kinesin binding protein complexed with Kif15 motor domain	<a href="http://www.rcsb.org/structure/6ZPH">http://www.rcsb.org/structure/6ZPH</a>	RCSB Protein Data Bank, 6ZPH
Atherton J, Hummel JJA, Olieric N, Locke J, Peña A, Rosenfeld SS, Steinmetz MO, Hoogenraad CC, Moores CA	2020	Kinesin binding protein complexed with Kif15 motor domain. Symmetrised asymmetric unit.	<a href="http://www.rcsb.org/structure/6ZPI">http://www.rcsb.org/structure/6ZPI</a>	RCSB Protein Data Bank, 6ZPI
Atherton J, Hummel JJA, Olieric N, Locke J, Peña A, Rosenfeld SS, Steinmetz MO, Hoogenraad CC, Moores CA	2020	Kinesin binding protein (KBP)	<a href="https://www.ebi.ac.uk/pdbe/emdb/EMD-11338">https://www.ebi.ac.uk/pdbe/emdb/EMD-11338</a>	Electron Microscopy Data Bank, EMD-11338
Atherton J, Hummel JJA, Olieric N, Locke J, Peña A, Rosenfeld SS, Steinmetz MO, Hoogenraad CC, Moores CA	2020	Kinesin binding protein complexed with Kif15 motor domain	<a href="https://www.ebi.ac.uk/pdbe/emdb/EMD-11339">https://www.ebi.ac.uk/pdbe/emdb/EMD-11339</a>	Electron Microscopy Data Bank, EMD-11339
Atherton J, Hummel JJA, Olieric N, Locke J, Peña A, Rosenfeld SS, Steinmetz MO, Hoogenraad CC, Moores CA	2020	Kinesin binding protein complexed with Kif15 motor domain. Symmetrised asymmetric unit.	<a href="https://www.ebi.ac.uk/pdbe/emdb/EMD-11340">https://www.ebi.ac.uk/pdbe/emdb/EMD-11340</a>	Electron Microscopy Data Bank, EMD-11340

## References

Afonine PV, Poon BK, Read RJ, Sobolev OV, Terwilliger TC, Urzhumtsev A, Adams PD. 2018. Real-space refinement in PHENIX for cryo-EM and crystallography. *Acta Crystallographica. Section D, Structural Biology* **74**:531–544. DOI: <https://doi.org/10.1107/S2059798318006551>, PMID: 29872004

- Alves MM**, Burzynski G, Delalande JM, Osinga J, van der Goot A, Dolga AM, de Graaff E, Brooks AS, Metzger M, Eisel UL, Shepherd I, Eggen BJ, Hofstra RM. 2010. KBP interacts with SCG10, linking Goldberg-Shprintzen syndrome to microtubule dynamics and neuronal differentiation. *Human Molecular Genetics* **19**:3642–3651. DOI: <https://doi.org/10.1093/hmg/ddq280>, PMID: 20621975
- Atherton J**, Farabella I, Yu IM, Rosenfeld SS, Houdusse A, Topf M, Moores CA. 2014. Conserved mechanisms of microtubule-stimulated ADP release, ATP binding, and force generation in transport kinesins. *eLife* **3**:e03680. DOI: <https://doi.org/10.7554/eLife.03680>, PMID: 25209998
- Atherton J**, Yu IM, Cook A, Muretta JM, Joseph A, Major J, Sourigues Y, Clause J, Topf M, Rosenfeld SS, Houdusse A, Moores CA. 2017. The divergent mitotic kinesin MKLP2 exhibits atypical structure and mechanochemistry. *eLife* **6**:e27793. DOI: <https://doi.org/10.7554/eLife.27793>, PMID: 28826477
- Atherton J**, Luo Y, Xiang S, Yang C, Rai A, Jiang K, Stangier M, Vemu A, Cook AD, Wang S, Roll-Mecak A, Steinmetz MO, Akhmanova A, Baldus M, Moores CA. 2019. Structural determinants of microtubule minus end preference in CAMSAP CKK domains. *Nature Communications* **10**:5236. DOI: <https://doi.org/10.1038/s41467-019-13247-6>, PMID: 31748546
- Bell JM**, Chen M, Durmaz T, Fluty AC, Ludtke SJ. 2018. New software tools in EMAN2 inspired by EMDatabank map challenge. *Journal of Structural Biology* **204**:283–290. DOI: <https://doi.org/10.1016/j.jsb.2018.09.002>, PMID: 30189321
- Brooks AS**, Bertoli-Avella AM, Burzynski GM, Breedveld GJ, Osinga J, Boven LG, Hurst JA, Mancini GM, Lequin MH, de Coo RF, Matera I, de Graaff E, Meijers C, Willems PJ, Tibboel D, Oostra BA, Hofstra RM. 2005. Homozygous nonsense mutations in KIAA1279 are associated with malformations of the central and enteric nervous systems. *The American Journal of Human Genetics* **77**:120–126. DOI: <https://doi.org/10.1086/431244>, PMID: 15883926
- Brouwers N**, Mallol Martinez N, Vernos I. 2017. Role of Kif15 and its novel mitotic partner KBP in K-fiber dynamics and chromosome alignment. *PLOS ONE* **12**:e0174819. DOI: <https://doi.org/10.1371/journal.pone.0174819>, PMID: 28445502
- Chang HY**, Cheng HY, Tsao AN, Liu C, Tsai JW. 2019. Multiple functions of KBP in neural development underlie brain anomalies in Goldberg-Shprintzen syndrome. *Frontiers in Molecular Neuroscience* **12**:265. DOI: <https://doi.org/10.3389/fnmol.2019.00265>, PMID: 31736709
- Chen VB**, Arendall WB, Headd JJ, Keedy DA, Immormino RM, Kapral GJ, Murray LW, Richardson JS, Richardson DC. 2010. MolProbity: all-atom structure validation for macromolecular crystallography. *Acta Crystallographica Section D Biological Crystallography* **66**:12–21. DOI: <https://doi.org/10.1107/S090744490402073>, PMID: 20057044
- Chen S**, McMullan G, Faruqi AR, Murshudov GN, Short JM, Scheres SH, Henderson R. 2013. High-resolution noise substitution to measure overfitting and validate resolution in 3D structure determination by single particle electron cryomicroscopy. *Ultramicroscopy* **135**:24–35. DOI: <https://doi.org/10.1016/j.ultramic.2013.06.004>, PMID: 23872039
- Cheng K**, Wilkinson M, Chaban Y, Wigley DB. 2020. A conformational switch in response to chi converts RecBCD from phage destruction to DNA repair. *Nature Structural & Molecular Biology* **27**:71–77. DOI: <https://doi.org/10.1038/s41594-019-0355-2>, PMID: 31907455
- Cook AD**, Manka SW, Wang S, Moores CA, Atherton J. 2020. A microtubule RELION-based pipeline for cryo-EM image processing. *Journal of Structural Biology* **209**:107402. DOI: <https://doi.org/10.1016/j.jsb.2019.10.004>, PMID: 31610239
- Cross JA**, Dodding MP. 2019. Motor-cargo adaptors at the organelle-cytoskeleton interface. *Current Opinion in Cell Biology* **59**:16–23. DOI: <https://doi.org/10.1016/j.ccb.2019.02.010>, PMID: 30952037
- Culurgioni S**, Alfieri A, Pendolino V, Laddomada F, Mapelli M. 2011. Inscuteable and NuMA proteins bind competitively to Leu-Gly-Asn repeat-enriched protein (LGN) during asymmetric cell divisions. *PNAS* **108**:20998–21003. DOI: <https://doi.org/10.1073/pnas.1113077108>, PMID: 22171003
- Dafsari HS**, Byrne S, Lin JP, Pitt M, Jongbloed JD, Flinter F, Jungbluth H. 2015. Goldberg-Shprintzen megacolon syndrome with associated sensory motor axonal neuropathy. *American Journal of Medical Genetics Part A* **167**:1300–1304. DOI: <https://doi.org/10.1002/ajmg.a.36873>, PMID: 25846562
- Donato V**, Bonora M, Simoneschi D, Sartini D, Kudo Y, Saraf A, Florens L, Washburn MP, Stadtfeld M, Pinton P, Pagano M. 2017. The TDH-GCN5L1-Fbxo15-KBP Axis limits mitochondrial biogenesis in mouse embryonic stem cells. *Nature Cell Biology* **19**:341–351. DOI: <https://doi.org/10.1038/ncb3491>, PMID: 28319092
- Drerup CM**, Lusk S, Nechiporuk A. 2016. Kif1B interacts with KBP to promote axon elongation by localizing a microtubule regulator to growth cones. *Journal of Neuroscience* **36**:7014–7026. DOI: <https://doi.org/10.1523/JNEUROSCI.0054-16.2016>, PMID: 27358458
- Drévilion L**, Megarbane A, Demeer B, Matar C, Benit P, Briand-Suleau A, Bodereau V, Ghomid J, Nasser M, Decrouy X, Doco-Fenzy M, Rustin P, Gaillard D, Goossens M, Giurgea I. 2013. KBP-cytoskeleton interactions underlie developmental anomalies in Goldberg-Shprintzen syndrome. *Human Molecular Genetics* **22**:2387–2399. DOI: <https://doi.org/10.1093/hmg/ddt083>, PMID: 23427148
- Drozdetskiy A**, Cole C, Procter J, Barton GJ. 2015. JPred4: a protein secondary structure prediction server. *Nucleic Acids Research* **43**:W389–W394. DOI: <https://doi.org/10.1093/nar/gkv332>, PMID: 25883141
- Emsley P**, Cowtan K. 2004. Coot: model-building tools for molecular graphics. *Acta Crystallographica. Section D, Biological Crystallography* **60**:2126–2132. DOI: <https://doi.org/10.1107/S0907444904019158>, PMID: 15572765
- Fan X**, Wang J, Zhang X, Yang Z, Zhang JC, Zhao L, Peng HL, Lei J, Wang HW. 2019. Single particle cryo-EM reconstruction of 52 kDa streptavidin at 3.2 Å resolution. *Nature Communications* **10**:2386. DOI: <https://doi.org/10.1038/s41467-019-10368-w>, PMID: 31160591

- Geourjon C**, Deléage G. 1995. SOPMA: significant improvements in protein secondary structure prediction by consensus prediction from multiple alignments. *Bioinformatics* **11**:681–684. DOI: <https://doi.org/10.1093/bioinformatics/11.6.681>, PMID: 8808585
- Gigant B**, Wang W, Dreier B, Jiang Q, Pecqueur L, Plückthun A, Wang C, Knossow M. 2013. Structure of a kinesin-tubulin complex and implications for kinesin motility. *Nature Structural & Molecular Biology* **20**:1001–1007. DOI: <https://doi.org/10.1038/nsmb.2624>, PMID: 23872990
- Goddard TD**, Huang CC, Meng EC, Pettersen EF, Couch GS, Morris JH, Ferrin TE. 2018. UCSF ChimeraX: meeting modern challenges in visualization and analysis. *Protein Science* **27**:14–25. DOI: <https://doi.org/10.1002/pro.3235>, PMID: 28710774
- Grant T**, Rohou A, Grigorieff N. 2018. cisTEM, user-friendly software for single-particle image processing. *eLife* **7**:e35383. DOI: <https://doi.org/10.7554/eLife.35383>, PMID: 29513216
- Herzik MA**, Wu M, Lander GC. 2019. High-resolution structure determination of sub-100 kDa complexes using conventional cryo-EM. *Nature Communications* **10**:1032. DOI: <https://doi.org/10.1038/s41467-019-08991-8>, PMID: 30833564
- Hildebrand A**, Remmert M, Biegert A, Söding J. 2009. Fast and accurate automatic structure prediction with HHpred. *Proteins: Structure, Function, and Bioinformatics* **77**:128–132. DOI: <https://doi.org/10.1002/prot.22499>, PMID: 19626712
- Hirokawa N**, Noda Y, Tanaka Y, Niwa S. 2009. Kinesin superfamily motor proteins and intracellular transport. *Nature Reviews Molecular Cell Biology* **10**:682–696. DOI: <https://doi.org/10.1038/nrm2774>
- Hirokawa N**, Niwa S, Tanaka Y. 2010. Molecular motors in neurons: transport mechanisms and roles in brain function, development, and disease. *Neuron* **68**:610–638. DOI: <https://doi.org/10.1016/j.neuron.2010.09.039>, PMID: 21092854
- Hirst CS**, Stamp LA, Bergner AJ, Hao MM, Tran MX, Morgan JM, Dutschmann M, Allen AM, Paxinos G, Furlong TM, McKeown SJ, Young HM. 2017. Kif1bp loss in mice leads to defects in the peripheral and central nervous system and perinatal death. *Scientific Reports* **7**:16676. DOI: <https://doi.org/10.1038/s41598-017-16965-3>, PMID: 29192291
- Karpenahalli MR**, Lupas AN, Söding J. 2007. TPRpred: a tool for prediction of TPR-, PPR- and SEL1-like repeats from protein sequences. *BMC Bioinformatics* **8**:2. DOI: <https://doi.org/10.1186/1471-2105-8-2>, PMID: 17199898
- Kellogg EH**, Hejab NMA, Howes S, Northcote P, Miller JH, Díaz JF, Downing KH, Nogales E. 2017. Insights into the distinct mechanisms of action of taxane and Non-Taxane microtubule stabilizers from Cryo-EM structures. *Journal of Molecular Biology* **429**:633–646. DOI: <https://doi.org/10.1016/j.jmb.2017.01.001>, PMID: 28104363
- Kevenaar JT**, Bianchi S, van Spronsen M, Olieric N, Lipka J, Frias CP, Mikhaylova M, Harterink M, Keijzer N, Wulf PS, Hilbert M, Kapitein LC, de Graaff E, Ahkmanova A, Steinmetz MO, Hoogenraad CC. 2016. Kinesin-Binding protein controls microtubule dynamics and cargo trafficking by regulating kinesin motor activity. *Current Biology* **26**:849–861. DOI: <https://doi.org/10.1016/j.cub.2016.01.048>, PMID: 26948876
- Khoshouei M**, Radjainia M, Baumeister W, Danev R. 2017. Cryo-EM structure of haemoglobin at 3.2 Å determined with the volta phase plate. *Nature Communications* **8**:16099. DOI: <https://doi.org/10.1038/ncomms16099>, PMID: 28665412
- Klejnot M**, Falnikar A, Ulaganathan V, Cross RA, Baas PW, Kozielski F. 2014. The crystal structure and biochemical characterization of Kif15: a bifunctional molecular motor involved in bipolar spindle formation and neuronal development. *Acta Crystallographica Section D Biological Crystallography* **70**:123–133. DOI: <https://doi.org/10.1107/S1399004713028721>, PMID: 24419385
- Klinman E**, Holzbaur ELF. 2018. Walking forward with kinesin. *Trends in Neurosciences* **41**:555–556. DOI: <https://doi.org/10.1016/j.tins.2018.07.006>, PMID: 30143179
- Lawrence CJ**, Dawe RK, Christie KR, Cleveland DW, Dawson SC, Endow SA, Goldstein LS, Goodson HV, Hirokawa N, Howard J, Malmberg RL, McIntosh JR, Miki H, Mitchison TJ, Okada Y, Reddy AS, Saxton WM, Schliwa M, Scholey JM, Vale RD, et al. 2004. A standardized kinesin nomenclature. *Journal of Cell Biology* **167**:19–22. DOI: <https://doi.org/10.1083/jcb.200408113>, PMID: 15479732
- Lehti MS**, Kotaja N, Sironen A. 2015. KIF1-binding protein interacts with KIF3A in haploid male germ cells. *Reproduction* **150**:209–216. DOI: <https://doi.org/10.1530/REP-15-0173>, PMID: 26245936
- Lyons DA**, Naylor SG, Mercurio S, Dominguez C, Talbot WS. 2008. KBP is essential for axonal structure, outgrowth and maintenance in zebrafish, providing insight into the cellular basis of Goldberg-Shprintzen syndrome. *Development* **135**:599–608. DOI: <https://doi.org/10.1242/dev.012377>, PMID: 18192286
- MacKenzie KC**, de Graaf BM, Syrimis A, Zhao Y, Brosens E, Mancini GMS, Schot R, Halley D, Wilke M, Vølle A, Flinter F, Green A, Mansour S, Pilch J, Stark Z, Zamba-Papanicolaou E, Christophidou-Anastasiadou V, Hofstra RMW, Jongbloed JDH, Nicolaou N, et al. 2020. Goldberg-Shprintzen syndrome is determined by the absence, or reduced expression levels, of KIFBP. *Human Mutation* **41**:1906–1917. DOI: <https://doi.org/10.1002/humu.24097>, PMID: 32939943
- Malaby HLH**, Dumas ME, Ohi R, Stumpff J. 2019. Kinesin-binding protein ensures accurate chromosome segregation by buffering KIF18A and KIF15. *Journal of Cell Biology* **218**:1218–1234. DOI: <https://doi.org/10.1083/jcb.201806195>, PMID: 30709852
- Mandelkow E**, Mandelkow EM. 2002. Kinesin motors and disease. *Trends in Cell Biology* **12**:585–591. DOI: [https://doi.org/10.1016/S0962-8924\(02\)02400-5](https://doi.org/10.1016/S0962-8924(02)02400-5), PMID: 12495847
- Merk A**, Bartesaghi A, Banerjee S, Falconieri V, Rao P, Davis MI, Pragari R, Boxer MB, Earl LA, Milne JLS, Subramaniam S. 2016. Breaking Cryo-EM resolution barriers to facilitate drug discovery. *Cell* **165**:1698–1707. DOI: <https://doi.org/10.1016/j.cell.2016.05.040>, PMID: 27238019

- Miki H**, Setou M, Kaneshiro K, Hirokawa N. 2001. All kinesin superfamily protein, KIF, genes in mouse and human. *PNAS* **98**:7004–7011. DOI: <https://doi.org/10.1073/pnas.111145398>, PMID: 11416179
- Parke CL**, Wojcik EJ, Kim S, Worthylake DK. 2010. ATP hydrolysis in Eg5 kinesin involves a catalytic two-water mechanism. *Journal of Biological Chemistry* **285**:5859–5867. DOI: <https://doi.org/10.1074/jbc.M109.071233>, PMID: 20018897
- Peña A**, Sweeney A, Cook AD, Locke J, Topf M, Moores CA. 2020. Structure of Microtubule-Trapped human Kinesin-5 and its mechanism of inhibition revealed using cryoelectron microscopy. *Structure* **28**:450–457. DOI: <https://doi.org/10.1016/j.str.2020.01.013>, PMID: 32084356
- Perez-Riba A**, Itzhaki LS. 2019. The tetratricopeptide-repeat motif is a versatile platform that enables diverse modes of molecular recognition. *Current Opinion in Structural Biology* **54**:43–49. DOI: <https://doi.org/10.1016/j.sbi.2018.12.004>, PMID: 30708253
- Pernigo S**, Chegkazi MS, Yip YY, Treacy C, Glorani G, Hansen K, Politis A, Bui S, Dodding MP, Steiner RA. 2018. Structural basis for isoform-specific kinesin-1 recognition of Y-acidic cargo adaptors. *eLife* **7**:e38362. DOI: <https://doi.org/10.7554/eLife.38362>, PMID: 30320553
- Pettersen EF**, Goddard TD, Huang CC, Couch GS, Greenblatt DM, Meng EC, Ferrin TE. 2004. UCSF chimera—a visualization system for exploratory research and analysis. *Journal of Computational Chemistry* **25**:1605–1612. DOI: <https://doi.org/10.1002/jcc.20084>, PMID: 15264254
- Punjani A**, Rubinstein JL, Fleet DJ, Brubaker MA. 2017. cryoSPARC: algorithms for rapid unsupervised cryo-EM structure determination. *Nature Methods* **14**:290–296. DOI: <https://doi.org/10.1038/nmeth.4169>, PMID: 28165473
- Quinaud M**, Plé S, Job V, Contreras-Martel C, Simorre JP, Attree I, Dessen A. 2007. Structure of the heterotrimeric complex that regulates type III secretion needle formation. *PNAS* **104**:7803–7808. DOI: <https://doi.org/10.1073/pnas.0610098104>, PMID: 17470796
- Randall TS**, Yip YY, Wallock-Richards DJ, Pfisterer K, Sanger A, Ficek W, Steiner RA, Bevil AJ, Parsons M, Dodding MP. 2017. A small-molecule activator of kinesin-1 drives remodeling of the microtubule network. *PNAS* **114**:13738–13743. DOI: <https://doi.org/10.1073/pnas.1715115115>, PMID: 29229862
- Ren J**, Wang S, Chen H, Wang W, Huo L, Feng W. 2018. Coiled-coil 1-mediated fastening of the neck and motor domains for kinesin-3 autoinhibition. *PNAS* **115**:E11933–E11942. DOI: <https://doi.org/10.1073/pnas.1811209115>, PMID: 30463954
- Rosenfeld SS**, Xing J, Jefferson GM, King PH. 2005. Docking and rolling, a model of how the mitotic motor Eg5 works. *Journal of Biological Chemistry* **280**:35684–35695. DOI: <https://doi.org/10.1074/jbc.M506561200>, PMID: 16115880
- Roy A**, Kucukural A, Zhang Y. 2010. I-TASSER: a unified platform for automated protein structure and function prediction. *Nature Protocols* **5**:725–738. DOI: <https://doi.org/10.1038/nprot.2010.5>, PMID: 20360767
- Salehpour S**, Hashemi-Gorji F, Soltani Z, Ghafouri-Fard S, Miryounesi M. 2017. Association of a novel nonsense mutation in KIAA1279 with Goldberg-Shprintzen syndrome. *Iranian Journal of Child Neurology* **11**:70–74. PMID: 28277559
- Sali A**, Blundell TL. 1993. Comparative protein modelling by satisfaction of spatial restraints. *Journal of Molecular Biology* **234**:779–815. DOI: <https://doi.org/10.1006/jmbi.1993.1626>, PMID: 8254673
- Scarabelli G**, Grant BJ. 2013. Mapping the structural and dynamical features of kinesin motor domains. *PLoS Computational Biology* **9**:e1003329. DOI: <https://doi.org/10.1371/journal.pcbi.1003329>, PMID: 24244137
- Schindelin J**, Arganda-Carreras I, Frise E, Kaynig V, Longair M, Pietzsch T, Preibisch S, Rueden C, Saalfeld S, Schmid B, Tinevez JY, White DJ, Hartenstein V, Eliceiri K, Tomancak P, Cardona A. 2012. Fiji: an open-source platform for biological-image analysis. *Nature Methods* **9**:676–682. DOI: <https://doi.org/10.1038/nmeth.2019>, PMID: 22743772
- Shang Z**, Zhou K, Xu C, Csencsits R, Cochran JC, Sindelar CV. 2014. High-resolution structures of kinesin on microtubules provide a basis for nucleotide-gated force-generation. *eLife* **3**:e04686. DOI: <https://doi.org/10.7554/eLife.04686>, PMID: 25415053
- Sievers F**, Wilm A, Dineen D, Gibson TJ, Karplus K, Li W, Lopez R, McWilliam H, Remmert M, Söding J, Thompson JD, Higgins DG. 2011. Fast, scalable generation of high-quality protein multiple sequence alignments using clustal omega. *Molecular Systems Biology* **7**:539. DOI: <https://doi.org/10.1038/msb.2011.75>, PMID: 21988835
- Suo C**, Deng W, Vu TN, Li M, Shi L, Pawitan Y. 2018. Accumulation of potential driver genes with genomic alterations predicts survival of high-risk neuroblastoma patients. *Biology Direct* **13**:14. DOI: <https://doi.org/10.1186/s13062-018-0218-5>, PMID: 30012197
- Tanaka H**, Ito J, Cho K, Mikawa M. 1993. Hirschsprung disease, unusual face, mental retardation, epilepsy, and congenital heart disease: goldberg-shprintzen syndrome. *Pediatric Neurology* **9**:479–481. DOI: [https://doi.org/10.1016/0887-8994\(93\)90029-C](https://doi.org/10.1016/0887-8994(93)90029-C), PMID: 7605558
- Topf M**, Lasker K, Webb B, Wolfson H, Chiu W, Sali A. 2008. Protein structure fitting and refinement guided by cryo-EM density. *Structure* **16**:295–307. DOI: <https://doi.org/10.1016/j.str.2007.11.016>, PMID: 18275820
- Vale RD**. 2003. The molecular motor toolbox for intracellular transport. *Cell* **112**:467–480. DOI: [https://doi.org/10.1016/S0092-8674\(03\)00111-9](https://doi.org/10.1016/S0092-8674(03)00111-9), PMID: 12600311
- Valence S**, Poirier K, Lebrun N, Saillour Y, Sonigo P, Bessières B, Attié-Bitach T, Benachi A, Masson C, Encha-Razavi F, Chelly J, Bahi-Buisson N. 2013. Homozygous truncating mutation of the KBP gene, encoding a KIF1B-binding protein, in a familial case of fetal polymicrogyria. *Neurogenetics* **14**:215–224. DOI: <https://doi.org/10.1007/s10048-013-0373-x>, PMID: 24072599

- van der Vaart B**, van Riel WE, Doodhi H, Kevenaer JT, Katrukha EA, Gumy L, Bouchet BP, Grigoriev I, Spangler SA, Yu KL, Wulf PS, Wu J, Lansbergen G, van Battum EY, Pasterkamp RJ, Mimori-Kiyosue Y, Demmers J, Olieric N, Maly IV, Hoogenraad CC, et al. 2013. CFEOM1-associated kinesin KIF21A is a cortical microtubule growth inhibitor. *Developmental Cell* **27**:145–160. DOI: <https://doi.org/10.1016/j.devcel.2013.09.010>, PMID: 24120883
- Wang J**, Dye BT, Rajashankar KR, Kurinov I, Schulman BA. 2009. Insights into anaphase promoting complex TPR subdomain assembly from a CDC26-APC6 structure. *Nature Structural & Molecular Biology* **16**:987–989. DOI: <https://doi.org/10.1038/nsmb.1645>, PMID: 19668213
- Wang D**, Nitta R, Morikawa M, Yajima H, Inoue S, Shigematsu H, Kikkawa M, Hirokawa N. 2016a. Motility and microtubule depolymerization mechanisms of the Kinesin-8 motor, KIF19A. *eLife* **5**:e18101. DOI: <https://doi.org/10.7554/eLife.18101>, PMID: 27690357
- Wang S**, Li W, Liu S, Xu J. 2016b. RaptorX-Property: a web server for protein structure property prediction. *Nucleic Acids Research* **44**:W430–W435. DOI: <https://doi.org/10.1093/nar/gkw306>, PMID: 27112573
- Wozniak MJ**, Melzer M, Dorner C, Haring HU, Lammers R. 2005. The novel protein KBP regulates mitochondria localization by interaction with a kinesin-like protein. *BMC Cell Biology* **6**:35. DOI: <https://doi.org/10.1186/1471-2121-6-35>, PMID: 16225668
- Yan R**, Xu D, Yang J, Walker S, Zhang Y. 2013. A comparative assessment and analysis of 20 representative sequence alignment methods for protein structure prediction. *Scientific Reports* **3**:2619. DOI: <https://doi.org/10.1038/srep02619>, PMID: 24018415
- Yang Y**, Heffernan R, Paliwal K, Lyons J, Dehzangi A, Sharma A, Wang J, Sattar A, Zhou Y. 2017. SPIDER2: a package to predict secondary structure, accessible surface area, and Main-Chain torsional angles by deep neural networks. *Methods in Molecular Biology* **1484**:55–63. DOI: [https://doi.org/10.1007/978-1-4939-6406-2\\_6](https://doi.org/10.1007/978-1-4939-6406-2_6), PMID: 27787820
- Zeytuni N**, Zarivach R. 2012. Structural and functional discussion of the tetra-trico-peptide repeat, a protein interaction module. *Structure* **20**:397–405. DOI: <https://doi.org/10.1016/j.str.2012.01.006>, PMID: 22404999
- Zhang K**. 2016. Gctf: real-time CTF determination and correction. *Journal of Structural Biology* **193**:1–12. DOI: <https://doi.org/10.1016/j.jsb.2015.11.003>, PMID: 26592709
- Zhang K**, Keane SC, Su Z, Irobalieva RN, Chen M, Van V, Sciandra CA, Marchant J, Heng X, Schmid MF, Case DA, Ludtke SJ, Summers MF, Chiu W. 2018. Structure of the 30 kDa HIV-1 RNA Dimerization Signal by a Hybrid Cryo-EM, NMR, and Molecular Dynamics Approach. *Structure* **26**:490–498. DOI: <https://doi.org/10.1016/j.str.2018.01.001>, PMID: 29398526
- Zheng SQ**, Palovcak E, Armache JP, Verba KA, Cheng Y, Agard DA. 2017. MotionCor2: anisotropic correction of beam-induced motion for improved cryo-electron microscopy. *Nature Methods* **14**:331–332. DOI: <https://doi.org/10.1038/nmeth.4193>, PMID: 28250466
- Zimmermann L**, Stephens A, Nam SZ, Rau D, Kübler J, Lozajic M, Gabler F, Söding J, Lupas AN, Alva V. 2018. A completely reimplemented MPI bioinformatics toolkit with a new HHpred server at its core. *Journal of Molecular Biology* **430**:2237–2243. DOI: <https://doi.org/10.1016/j.jmb.2017.12.007>, PMID: 29258817
- Zivanov J**, Nakane T, Forsberg BO, Kimanius D, Hagen WJ, Lindahl E, Scheres SH. 2018. New tools for automated high-resolution cryo-EM structure determination in RELION-3. *eLife* **7**:e42166. DOI: <https://doi.org/10.7554/eLife.42166>, PMID: 30412051